

The 2012 Sumatra great earthquake sequence

Zacharie Duputel^{1*}, Hiroo Kanamori¹, Victor C. Tsai¹, Luis Rivera²,
Lingsen Meng¹, Jean-Paul Ampuero¹ and Joann M. Stock¹.

(1) Seismological Laboratory, California Institute of Technology, 1200E.
California Blvd., Pasadena, California 91125, USA.

(2) IPGS-EOST, CNRS/Université de Strasbourg, UMR 7516, 5 rue René
Descartes, 67084 Strasbourg Cedex, France.

* To whom the correspondence should be addressed: zacharie@gps.caltech.edu
tel: +1 626-395-3801

1 **Abstract**

2 The equatorial Indian Ocean is a well known place of active intraplate
3 deformation defying the conventional view of rigid plates separated by narrow
4 boundaries where deformation is confined. On 11 April 2012, this region was hit
5 in a couple of hours by two of the largest strike-slip earthquakes ever recorded
6 (moment magnitudes $M_w=8.6$ and $M_w=8.2$). Broadband seismological
7 observations of the $M_w=8.6$ mainshock indicate a large centroid depth ($\sim 30\text{km}$)
8 and remarkable rupture complexity. Detailed study of the surface-wave
9 directivity and moment rate functions clearly indicates the partition of the
10 rupture into at least two distinct subevents. To account for these observations,
11 we developed a procedure to invert for multiple-point-source parameters. The
12 optimum source model at long period consists of two point sources separated by
13 about 209 km with magnitudes $M_w=8.5$ and $M_w=8.3$. To explain the remaining
14 discrepancies between predicted and observed surface waves, we can refine this
15 model by adding directivity along the WNW-ESE axis. However, we do not
16 exclude more complicated models. To analyze the $M_w=8.2$ aftershock, we
17 removed the perturbation due to large surface-wave arrivals of the $M_w=8.6$
18 mainshock by subtracting the corresponding synthetics computed for the two-
19 subevent model. Analysis of the surface-wave amplitudes suggests that the
20 $M_w=8.2$ aftershock had a large centroid depth between 30 km and 40 km. This
21 major earthquake sequence brings a new perspective to the seismotectonics of
22 the equatorial Indian Ocean and reveals active deep lithospheric deformations.

23

24

25 **Keywords**

26 2012 Sumatra earthquake sequence; Intraplate earthquakes; Earthquake source
27 observations; Seismicity and tectonics; Surface waves and free oscillations

28

29 **1. Introduction**

30 Great strike-slip earthquakes are very uncommon, with the most well-known
31 recent events being the Mw=7.8 2001 Kunlun earthquake, the Mw=7.9 2002
32 Denali earthquake and the Mw=8.1 2004 Macquarie Island earthquake (Tsuboi
33 et al., 2003; Tocheport et al., 2006; Hayes et al., 2009; Duputel et al., 2012). Other
34 large events are also reported in the first half of the 20th century, including the
35 two major M~8.0 1905 Mongolian earthquakes and the Ms=8.6 1950 Assam
36 earthquake, although details of their source characteristics are not known due to
37 the small number of observations (Ben-Menahem et al., 1974; Chen and Molnar,
38 1977; Okal, 1977; Schlupp and Cisternas, 2007). Yet it is known that many large
39 strike-slip earthquakes involve remarkable rupture complexity, and the Mw=8.1
40 1998 Balleny islands earthquake (Hjörleifsdóttir et al., 2009) serves as a good
41 example of this. The seismic data from this event can be explained by subevents
42 with different mechanisms (Henry et al., 2000). Rupture branching onto multiple
43 subfaults was also observed, for example, during the Mw=7.3 1992 Landers
44 earthquake, during the Mw=7.8 2001 Kunlun earthquake (Tocheport et al., 2006)
45 and, more recently, during the Mw=7.2 2010 El Mayor-Cucapah earthquake
46 (Hauksson et al., 2010).

47

48 The 2012 Sumatra great earthquake sequence is particularly interesting for
49 several reasons. First, with moment magnitudes $Mw \geq 8.2$, it consists of two of
50 the largest strike-slip earthquakes ever recorded, and among the largest
51 intraplate earthquakes on instrumental records. Secondly, this unusual series of
52 large intraplate earthquakes occurred in the oceanic lithosphere of the Cocos
53 Basin (equatorial Indian Ocean), which has a unique seismotectonic
54 environment. This region is bounded by the Sunda Megathrust to the north, the
55 Wharton Basin to the south, the Ninetyeast Ridge to the west and the
56 Investigator Fracture Zone to the east (Fig. 1). The whole area constitutes a
57 diffuse deformation zone which is currently interpreted as the boundary
58 separating the Indian and Australian Plates (Wiens et al., 1985; Deplus et al.,
59 1998; Delescluse and Chamot-Rooke, 2007; Demets et al., 2010). The 2012
60 Sumatra earthquake sequence began on 11 April 2012, when the $Mw=8.6$
61 Sumatra event occurred off the west coast of Northern Sumatra (8h 38min 37s
62 UTC - zero time used from here, $2.31^\circ N$, $93.06^\circ E$; U. S. Geological Survey - USGS),
63 about 400 km southwest of Aceh (Fig. 1). Another major $Mw=8.2$ earthquake
64 occurred 2 hours after the mainshock (10h 43min 9s UTC, $0.77^\circ N$, $92.45^\circ E$;
65 USGS), approximately 200 km to the south. These earthquakes were preceded by
66 a $Mw=7.3$ earthquake on 10 January 2012, located very close to the epicenter of
67 the mainshock.

68

69 The complexity of the $Mw=8.6$ Sumatra earthquake was detected early on by
70 preliminary source analyses (Hayes, 2012; Kiser and Ishii, 2012; Meng et al.,
71 2012; Shao et al., 2012; Wei, 2012). The intricate distribution of aftershocks, the
72 complexity of short-period body-wave waveforms and the remoteness of

73 geodetic instruments due to the oceanic epicenter location make it difficult to
74 resolve the rupture process in detail. On the other hand, seismic waves from the
75 2012 Sumatra earthquake sequence were recorded by hundreds of global
76 broadband seismographs, enabling robust characterization of the overall rupture
77 characteristics at long period. The goal of this work is to provide a reliable
78 description of the first-order source attributes of the mainshock and of its
79 aftershocks using long-period (100-500 s) and ultra-long-period (>500 s) data.
80 In the following, we analyze this complicated earthquake sequence using both
81 single-point-source characterization and multiple-point-source inversion. This
82 enables us to resolve distinct aspects of the mainshock rupture process.

83

84 **2. W phase Inversion for Point-Source Geometry**

85 Great earthquakes ($M_w > 8.0$) generally involve rupture propagation over large
86 distances in a few minutes. In such cases, the point-source approximation is only
87 valid for ultra-long-period seismic waves such as the W phase, which
88 corresponds to the superposition of the first overtones of the Earth normal
89 modes between 100 s and 1000 s (Kanamori, 1993). As shown in Fig. 1b, the W
90 phase is conspicuous between the P wave and the surface wave train on
91 broadband displacement records of the $M_w = 8.6$ 2012 Sumatra earthquake. The
92 W phase source-inversion algorithm was initially developed to provide rapid
93 characterization of the seismic source for tsunami warning purposes (Kanamori
94 and Rivera, 2008; Hayes, Rivera, et al., 2009; Duputel et al., 2011) and is a
95 reliable and straightforward method to resolve the first-order attributes of large
96 earthquakes (Tsai et al., 2011; Duputel et al., 2012). Point-source parameters of
97 all events with $M_w \geq 5.8$ during the 2012 Sumatra earthquake sequence were

98 inverted using the W phase algorithm. The deviatoric moment tensor
99 components as well as the centroid locations (latitudes, longitudes, depths) and
100 timings were resolved following the procedure described by Duputel et al.
101 (2012). The W phase solutions obtained in this study are presented in Fig. 1a.

102

103 For the Mw=8.6 mainshock, we inverted records of 66 broadband stations within
104 an epicentral distance of 90° for a point-source moment tensor. Most of the 113
105 selected channels are from ultra-long-period seismometers (STS-1) with low
106 noise level in the 200-1000 s passband used for the inversion. The solution is
107 shown in Fig. 1 (inset green mechanism) and examples of waveform fits are
108 included in the supplementary material (Fig. S1). The scalar moment is
109 estimated to be $M_0 = 9.2 \times 10^{21}$ N.m (Mw = 8.6) and the best double-couple nodal
110 planes have orientations given by strike $\phi = 199^\circ$, dip $\delta = 78^\circ$, rake $\lambda = 7^\circ$ (NNE-
111 SSW plane) and $\phi = 108^\circ$, $\delta = 83^\circ$, $\lambda = 168^\circ$ (WNW-ESE plane). The moment
112 tensor thus determined has a relatively small intermediate eigenvalue
113 (eigenvalues are $\lambda_1=8.74$, $\lambda_2=0.89$ and $\lambda_3=-9.63$ in units of 10^{28} N.m, $\varepsilon=$
114 $\lambda_2/\max(|\lambda_1|, |\lambda_3|)=-0.09$) compared to the Global CMT solution ($\lambda_1=8.10$, $\lambda_2=1.71$
115 and $\lambda_3=-9.81$ in units of 10^{28} N.m, $\varepsilon=-0.17$), which was obtained using mantle
116 waves with periods shorter than 200 s. Although the W phase solution does not
117 indicate any apparent complexity at ultra-long period (200-1000 s), the larger
118 non-double couple component in the Global CMT solution suggests a complicated
119 rupture process at shorter periods for the mainshock.

120

121 Source analysis of the Mw=8.2 aftershock is more complicated since long-period
122 waveforms are disturbed by the large amplitude arrivals of the Mw=8.6

123 mainshock, which occurred about 2 hours before. To handle this, we generated a
124 residual trace by subtracting the synthetics for the mainshock from the data.
125 Since the disturbances mostly correspond to R2, G2 and G3 wavetrains that are
126 sensitive to shallow lateral heterogeneities, the synthetics are computed using
127 the spectral-element method (SEM, Komatitsch and Tromp, 1999) for a 3D Earth
128 model composed of the mantle model S362ANI (Kustowski et al., 2008) and the
129 crustal model Crust 2.0 (Bassin et al., 2000). To account for the source
130 complexity of the mainshock, we used the two-point-source model presented in
131 section 5. We then inverted for a point-source moment tensor using the residuals
132 between observed seismograms and SEM synthetics in the 120-600 s passband
133 as the data vector. The solution shown in Fig. 1 (yellow mechanism) was
134 obtained using 26 stations with a well-balanced azimuthal distribution for which
135 examples of waveform fit is shown in Fig. S2. This inversion also yielded a small
136 intermediate eigenvalue (eigenvalues are $\lambda_1=2.28$, $\lambda_2=0.07$ and $\lambda_3=-2.35$ in units
137 of 10^{28} N.m, $\varepsilon=-0.03$). The scalar moment is $M_0 = 2.5 \times 10^{21}$ N.m ($M_w = 8.2$) and
138 the best double-couple nodal planes have orientations $\phi = 13^\circ$, $\delta = 86^\circ$, $\lambda = -1^\circ$
139 (NNE-SSW plane) and $\phi = 104^\circ$, $\delta = 89^\circ$, $\lambda = -176^\circ$ (WNW-ESE plane).
140
141 We also performed point-source inversions to determine the moment tensor of
142 the 10 January foreshock (blue mechanism in Fig. 1) and of the $5.8 \leq M_w < 8.2$
143 aftershocks through May 2012 (red mechanisms). Following the strategy of
144 Hayes et al. (2009), the passband is gradually shifted toward higher frequencies
145 for smaller earthquakes to reduce the effect of the long-period background noise
146 (cf., Duputel et al., 2012). The W phase solutions are in overall good agreement
147 with the Global CMT and USGS CMT solutions. They all indicate strike-slip

148 earthquakes except for two Mw=5.8 thrust events that occurred near the Sunda
149 trench on 20 April 2012 and 29 April 2012. It is difficult to infer anything about
150 the mainshock rupture orientation from these results. From the NNE-SSW trends
151 of the Ninetyeast ridge and fracture zones in the Cocos Basin, one might guess a
152 similar orientation for the main rupture. This assumption is reasonable in view
153 of the centroid location of the Mw=8.2 event with respect to the Mw=8.6
154 mainshock, but seems in contradiction with the many aftershocks located at the
155 western margin of the basin, including the Mw=6.2 earthquake on 15 April 2012
156 and the Mw=5.8 earthquake on 30 April 2012.

157

158 **3. Surface-wave directivity and radiation pattern**

159 The true fault plane orientation of the Mw=8.6 2012 Sumatra earthquake is
160 unclear. Preliminary finite fault inversions fail to discriminate which nodal plane
161 corresponds to the fault and the complex distribution of aftershocks presented in
162 Fig. 1 (also shown in Fig. S3 in the supplementary material) indicates two major
163 parallel WNW-ESE lineations separated by ~150 km and at least one additional
164 orthogonal NNE-SSW trend. For large earthquakes, long-period surface waves
165 can provide useful information on the source finiteness and rupture directivity.

166

167 To investigate the possible directivity effects of the Mw=8.6 mainshock,
168 seismograms were equalized to an epicentral distance of $\Delta_0=90^\circ$ using the
169 procedure described by Kanamori (1970). To do this, we retrieve the wavefield
170 $U(\omega, \Delta_0, \varphi)$ at distance Δ_0 and azimuth φ from the observations at distance Δ
171 using

172
$$U(\omega, \Delta_0, \varphi) = \left(\frac{\sin \Delta}{\sin \Delta_0} \right)^{\frac{1}{2}} U(\omega, \Delta, \varphi) \exp \left[i \left(\frac{\omega a (\Delta - \Delta_0)}{c} - \frac{m\pi}{2} \right) \right] \exp[\kappa(\Delta - \Delta_0)], \quad (1)$$

173 where m is the number of epicentral or antipodal passages in going from Δ to Δ_0 ,
174 and c and κ are respectively the phase velocity and attenuation coefficient as a
175 function of frequency. This operation ideally removes the differences in
176 propagation effects for different stations, so the amplitude as a function of
177 azimuth should reflect the source's radiation pattern. The values of c and κ used
178 for the equalization of the fundamental Love and Rayleigh waves are from the
179 PREM model (Dziewonski and Anderson, 1981). We exploited both the short arc
180 (R1, G1) and the long arc (R2, G2) wave trains to improve the azimuthal coverage
181 and measured root mean square (rms) amplitudes of equalized seismograms in
182 the 100-400 s passband. The result, presented as inset circular plots in Fig. 2a-b
183 and in Fig. S4-S5 in the supplementary material, shows quite simple radiation
184 patterns with deep (i.e., small amplitude) nodes and a clear asymmetry
185 suggesting directivity in the southwest direction.

186

187 To further analyze this apparent directivity, we measured the ratio between
188 observed and predicted surface-wave amplitudes in the 200-400 s passband. To
189 remove the effect of the mechanism, dispersion and attenuation, we used single-
190 point-source synthetic seismograms computed with the SEM method for a 3D
191 Earth model composed of the models S362ANI and Crust 2.0. We focus here on
192 the variation of the amplitude ratio (observed/predicted) as a function of
193 azimuth. The point-source solution indicates a strike-slip mechanism, which
194 produces four-lobed surface-wave radiation patterns with different orientations
195 for Love and Rayleigh waves (cf., inset circular plots in Fig. 2a-b). Small

196 amplitudes (and thus smaller signal-to-noise ratios) are expected in the nodal
197 azimuths of the surface-wave radiation patterns. We thus considered both
198 Rayleigh and Love waves which bring complementary information; we used
199 minor-arc (R1, G1) as well as major-arc (R2, G2) wave trains to improve the
200 azimuthal coverage of the radiation patterns. If there were no effect of finiteness,
201 the observed/predicted amplitude ratios would be unity for all azimuths. For the
202 Mw=8.6 2012 Sumatra earthquake, we clearly see in Fig. 2a and b that the
203 Rayleigh- and Love-wave amplitudes are enhanced in azimuths around 260° N
204 (i.e., 260° clockwise from north).

205

206 This directivity toward 260° N is not expected for rupture propagation along the
207 NNE-SSW or WNW-ESE nodal plane of the W phase or Global CMT point-source
208 solutions. This suggests geometric complexity of faulting or possible bias due to
209 structural heterogeneities unaccounted for in the considered 3D Earth model. To
210 test the validity of our amplitude ratio observations, we made the same
211 measurements for the Mw=7.3 10 January 2012 Sumatra foreshock for which the
212 W phase solution also indicates a strike-slip mechanism (blue mechanism in Fig.
213 1). Fig 2c and d show no anomalous azimuthal variations of the amplitude ratio
214 and indicate that the observed directivity patterns for the April 11 event are due
215 to source effects.

216

217 We also computed equalized seismograms and observed/predicted amplitude
218 ratios for the Mw=8.2 aftershock. As for the moment tensor calculation
219 presented in section 2, we used a residual trace by subtracting the synthetics for
220 the mainshock from the data in order to remove the long-period disturbances

221 generated by the Mw=8.6 mainshock. The equalization diagram and amplitude
222 ratios for the Mw=8.2 aftershock are presented in Fig. S6 and S7 in the
223 supplementary material. The rupture orientation is difficult to infer here since
224 there is no obvious directivity visible on the equalized seismograms and on the
225 observed/predicted amplitude ratios. The surface-wave radiation diagram is
226 remarkably simple which suggest a simpler rupture than that of the Mw=8.6
227 mainshock.

228

229 **4. Surface-wave moment rate functions**

230 To further investigate the directivity and complexity of the Mw=8.6 11 April
231 2012 earthquake, we computed broadband (periods of 25s-600s) minor-arc (R1)
232 Rayleigh-wave moment rate functions (MRFs). We removed the dispersive wave
233 propagation effects by deconvolving the data by point-source synthetic
234 seismograms computed for the Global CMT solution. We chose to use this
235 solution instead of the W phase CMT solution since the Global CMT synthetics
236 better fit the Rayleigh waves in the 25s-600s passband. An alternative approach
237 would be to use waveforms of the Mw=7.3 10 January foreshock as an empirical
238 Green's function. This technique, however, is limited at long period by the
239 background noise level, which can be large for a Mw=7.3 earthquake, and at
240 short period by the possible complexity of the moment rate function of the
241 foreshock. Such an empirical Green's function approach also has complications
242 due to differences in locations and focal mechanisms of the two events. To take
243 into account the effect of lateral structural variations, we used SEM synthetics
244 computed for a 3D Earth model (S362ANI and Crust2.0). We used the projected
245 Landweber deconvolution method (Bertero et al., 1999; Lanza et al., 1999)

246 imposing causality, positivity and a maximum rupture duration of 200 s. The R1
247 MRFs are shown in Fig. 3 as a function of the directivity parameter (Ruff, 1984;
248 Ammon et al., 2006), with the assumption of directivity toward 250° N, which
249 allows optimal alignment of the MRFs. Similar plots assuming rupture directivity
250 toward 235° N and 265° N are shown for comparison in the supplementary
251 material (Fig. S8 and S9). This operation allows us to transform any cosine
252 azimuthal moveout into a linear moveout. The directivity effect revealed by
253 surface-wave amplitudes is also visible here. The MRFs have large amplitudes
254 and short durations in the southwest direction and the total duration increases
255 with decreasing directivity parameter. We also found clear evidence of radiation
256 complexity. As the azimuth relative to the direction 250° N increases, a strong
257 second pulse shifts systematically to later times. The linear moveout of this
258 second pulse suggests rupture partitioning into at least two distinct subevents,
259 possibly aligned along an azimuth of about 250° N with respect to the Global
260 CMT centroid location. Other side lobes are observed around 70 s for a relative
261 azimuth of 180° and around 170 s for azimuths between 2° and 17°. However,
262 because of their relatively small amplitudes, it is difficult to associate them to
263 particular rupture features.

264

265 **5. Multiple-point-source analysis**

266 To account for the R1 MRFs observations that suggest two distinct subevents for
267 the Mw=8.6 mainshock, we performed a multiple-point-source inversion. We
268 simultaneously inverted the long-period data for the subevent moment tensors,
269 locations (latitudes, longitudes, depths), time delays and half durations using a
270 modified version of the Neighborhood Algorithm sampler (NA, Sambridge,

271 1999). The inversion is performed using the W phase at shorter periods than is
272 typically used for our single-point-source inversions of $M_w > 8.0$ earthquakes, to
273 better characterize the complexity of the rupture. This method has been
274 validated with several synthetic tests; for example, the same approach has been
275 successfully applied to the 2009 Samoa earthquake (cf. Fig. S10 in the
276 supplementary material). We discuss here the solutions obtained using the 150-
277 500 s passband.

278

279 Our preferred two-point-source model is included in Fig. 1 as the green
280 mechanisms and circles labeled I (first subevent) and II (second subevent). The
281 10200 locations in time and space explored after 50 NA iterations are shown by
282 circles in Fig. 4. Using the two distinct pulses observed on the R1 MRFs (Fig. 3)
283 for guidance, the point-source delays were sampled from 10 s to 40 s for the first
284 subevent and from 50 s to 120 s for the second subevent. Following the NA
285 procedure, higher sampling is made in regions associated with smaller misfits,
286 revealing two distinct clouds around the optimum locations for each subevent.
287 Although only W phase waveforms were used in the inversion, the waveform fits
288 of the surface waves are significantly improved using the two-point-source
289 model, as shown in Fig. 5. A systematic comparison between predicted
290 waveforms and observed seismograms is shown in the supplementary material
291 (Fig. S11-S14).

292

293 The first subevent has a centroid time delay of 36 s with respect to the origin
294 time and a moment of $M_0 = 8.0 \times 10^{21}$ N.m ($M_w=8.5$) that represents almost 70%
295 of the total moment. It is located very close to the single-point-source location

296 inferred from W phase and Global CMT results (2.22° N, 92.74° E). The second
297 subevent has a centroid time delay of 106 s, with a smaller scalar moment $M_0 =$
298 3.7×10^{21} N.m (Mw=8.3), and is located \sim 200 km southwest of the first subevent
299 (1.44° N, 91.04° E; see Fig. 1). The half durations for the first and second sources
300 are estimated to be 43 s and 70 s, respectively. This parameter is poorly
301 constrained by the inversion due to the long periods of the analyzed seismic
302 waves.

303

304 **6. Centroid depth**

305 As shown in Figs. 6a and b, with the relative size and spatial and temporal
306 distribution of the two point sources used to describe the mainshock rupture, the
307 computed radiation patterns can reproduce the overall directivity toward 260° N
308 shown in Figs. 2a and b. We can now use this model to determine a range of
309 reasonable centroid depths for the mainshock. Since there is almost no depth
310 dependence of sensitivity kernels for Love waves, we show the result for
311 Rayleigh waves (more details are provided in the supplementary material). Fig.
312 7 compares the amplitudes of the observed Rayleigh waves in the 200-600 s
313 passband with those of the two-point-source synthetics computed for depths
314 from 10 to 60 km. The synthetics are computed using SEM for a 3D Earth model
315 combining S362ANI and Crust 2.0, with a Moho depth of less than 10km in the
316 source region. It is clear that the centroid depth of 30 km can best explain
317 observed amplitudes (since the best-fit line to the observed and predicted
318 amplitudes – in red – most closely matches a 1:1 relationship shown with a
319 dashed line). Thus, the two-point-source model shown in Fig. 4 with a centroid

320 depth of 30 km is the long-period source model for the Mw=8.6 11 April Sumatra
321 earthquake that is constrained most objectively by the data.

322

323 We performed the same analysis to estimate the centroid depth of the Mw=8.2
324 aftershock. To eliminate the disturbances caused by the long-period surface-
325 wave arrivals of the Mw=8.6 mainshock , we substracted the SEM synthetics for
326 the two-point-source model from the data and used a shorter period passband
327 (100-400 s). Fig. 8 compares the observed Rayleigh waves amplitudes with those
328 of the SEM synthetics computed at different depths for the single-point-source
329 model presented in section 2 for the Mw=8.2 aftershock. This analysis suggests
330 that the Mw=8.2 11 April Sumatra earthquake occurred at a depth similar to the
331 Mw=8.6 mainshock, since the observed amplitudes are best explained by
332 centroid depths around 30 - 40 km.

333

334 **7. First-order determination of fault planes**

335 The two-point-source model presented so far for the Mw=8.6 mainshock is a
336 robust result and requires virtually no assumptions. However, we can refine our
337 model results by making a few reasonable assumptions. The surface-wave
338 radiation patterns shown in Fig. 6b suggest that slightly stronger directivity
339 toward 260° N would improve the match between the observed and computed
340 radiation patterns of both Love and Rayleigh waves. Since in the previous
341 analysis the temporal finiteness for each of the two point source is modeled by a
342 single MRF for all stations (i.e., an isosceles triangle), the only directivity for such
343 a model comes from the relative offset of the two subevents in space and time. A
344 simple way to improve the directivity fit toward 260° N is to replace the isosceles

345 MRF by an azimuthally dependent MRF of an asymmetric bilateral rupture using
346 a source finiteness function of the type introduced by Ben-Menahem (1961) and
347 Haskell (1963). The parameters involved are L1, fault length in the rupture
348 direction; L2, fault length in the opposite direction; V, rupture speed; and τ , the
349 local rise time. We assume that the slip distribution is uniform, $V=1.8$ km/s, and
350 $\tau = 25$ s. The rupture velocity was chosen to agree with preliminary finite-fault
351 inversion results (Hayes, 2012; Shao et al., 2012; Wei, 2012; Yue et al., 2012).
352 The relatively large τ assumed here reflects the large amount of slip resulting
353 from the large moment and the relatively small source dimension. Our objective
354 is to make a slight modification of the two-point-source model to better match
355 the observed radiation patterns using a model of simple asymmetric bilateral
356 faulting. We grid-searched for an optimum faulting orientation (assuming the
357 two possible fault strikes for each mechanism) and rupture propagation lengths,
358 L1 and L2. The explored parameters and the corresponding rms misfit values are
359 shown in Fig. S18. The optimum model shown in Fig. 6c corresponds to two
360 WNW-ESE parallel bilateral faults. Although the optimum model shows
361 asymmetric ruptures with a predominant propagation in the 288° N direction,
362 the absolute length of both fault segments for each subevent depends on the
363 assumed rupture speed, and are not constrained well. The optimum rupture
364 lengths are L1=100km, L2=40km for source I and L1=60km, L2=40km for source
365 II. On the other hand, the fault orientation is relatively well established here
366 since modification of the rupture azimuth for either of the two subfaults clearly
367 affects the predicted radiation patterns (cf. Fig. S17 and S18 in the
368 supplementary material). This result is consistent with the aftershock
369 distribution (cf. Fig. 1 and Fig. S3 in the supplementary material), which suggests

370 that slip was dominated by rupture on two subparallel WNW-ESE faults.

371

372 The partitioning of the rupture into distinct subevents can also be observed at
373 shorter periods. We computed stacks of P-wave coda envelopes in the 0.7-5 s
374 passband for epicentral distances of 30° to 95°. All vertical component traces
375 within this epicentral distance range are corrected for the instrument response
376 and bandpass filtered between 0.7 s and 5 s. The corresponding envelopes are
377 then aligned with respect to the P wave arrival and stacked in azimuth bins of
378 10°. All stacks of less than 3 channels are rejected. As shown in Fig. 9c, a discrete
379 phase can be easily tracked around 100 s after the P wave arrival for different
380 station azimuths. This is in good agreement with the timing of the second
381 subevent.

382

383 Meng et al. (2012) also performed back-projections of short period (1-2 s) P
384 waves from the Japanese Hi-Net network and European networks using the
385 MUSIC technique. The backprojection images and their interpretation are not the
386 main purpose of the current study and they are referenced here for comparison
387 with our long-period observations. The results obtained by Meng et al. (2012)
388 are presented in Fig. 9a and 9b. There is an overall good agreement between the
389 spatio-temporal positions of high-frequency radiation peaks and the proposed
390 two-subevent model. From back-projection images, Meng et al. (2012) proposed
391 the following complex rupture process presented in the inset scheme on Fig 9a.
392 The rupture initiated on a WNW-ESE fault (fault A) within the first 25 s after the
393 origin time, followed by a NNE-SSW bilateral rupture (fault B) up to 80 s after the
394 origin time. This was followed by a rupture along a second WNW-ESE fault (fault

395 C) located about 150 km south of the first fault (fault A). This stage lasts until
396 150 s after origin time when rupture ends on a parallel WNW-ESE fault (fault D)
397 close to the Ninetyeast ridge. Besides the clear pulse around 100 s visible on
398 stacks of P-wave coda envelopes (Fig. 9c), we also see other discrete, but less
399 coherent phases around 60 s and 180 s after the P arrival time which may be
400 related to the intermediate rupture on fault B and to the late WNW-ESE faulting
401 on fault D. However, the intermediate rupture on fault B and the late rupture on
402 fault D are not obvious in our long period results. We performed 3-point-source
403 inversions using different frequency bands (i.e., 120-400 s, 150-500 s and 200-
404 500 s) but they did not provide stable results, with the optimum location of the
405 two later subevents being randomly distributed in time and space. This could be
406 explained if the high-frequency radiators on faults B and D did not involve large
407 amounts of slip compared to WNW-ESE faulting on faults A and C; such disparity
408 between short-period and long-period radiation has already been observed for
409 large megathrust earthquakes such as the Mw=9.0 2011 Tohoku-oki earthquake
410 (Meng et al., 2011), the Mw=8.8 2010 Maule Chile earthquake (Kiser and Ishii,
411 2011) and the Mw=9.1 2004 Sumatra Earthquake (Lay et al., 2012). This
412 assumption is compatible with the finite-fault model proposed by Yue et al.
413 (2012) which suggests that the two main slip contributions are associated with
414 faults A and C, with smaller slip being associated with faults B and D. Although
415 the focal mechanism on the intermediate NNE-SSW fault (fault B) is still a matter
416 of debate, the surface-wave radiation pattern for the whole rupture shows very
417 clear and deep nodes (Fig. 2 and Fig. 6) which rules out any significant thrust or
418 normal subevents.

419

420 **8. Discussion and Conclusion**

421 Various seismological observations from high-frequency P waves to long-period
422 surface waves reveal a remarkable complexity in the early stages of the 2012
423 Sumatra earthquake sequence. Our analysis of long-period seismic waves yielded
424 a two-point-source model for the Mw=8.6 mainshock. The first subevent has a
425 magnitude of Mw=8.5 with a centroid time of 36 s after the origin time. The
426 second subevent has a magnitude of Mw=8.3 with a centroid time of 106s after
427 the origin time. The best-fit centroid depth is 30 km for both subevents. This
428 two-point-source model is currently the most robust zeroth-order model that
429 can explain the overall asymmetry of long-period (100-400 s) Rayleigh and Love
430 wave radiation patterns for the Mw=8.6 mainshock.

431

432 To explain the remaining discrepancy in the radiation patterns, we can invoke a
433 simple asymmetric bilateral rupture for both the first and the second subevents.
434 This model with simple parameterization involves two parallel WNW-ESE faults
435 separated by about 150 km, shown in Fig. 6c. This interpretation of a dominant
436 slip contribution from two parallel WNW-ESE faults is compatible with the MRF
437 back-projection and with the slip model proposed by Yue et al. (2012). Such fault
438 orientations have been previously observed on multibeam bathymetry and
439 seismic reflection profiles along the Ninetyeast Ridge (Sager et al., 2010; Meng et
440 al., 2012) and are in good agreement with the distribution of aftershocks, which
441 highlight two clear parallel WNW-ESE trends. These WNW-ESE oriented
442 ruptures are also very consistent with the predicted motion of the Australian
443 Plate relative to the Indian Plate of about 13 mm/yr in the direction of 316° N
444 (white arrows on Fig. 1 , Demets et al., 2010).

445

446 From the relative centroid locations we obtained for the Mw=8.6 mainshock and
447 the Mw=8.2 aftershock, and from the NNE-SSW lineations of the fracture zones in
448 the Cocos Basin, one might theorize that the main rupture would have occurred
449 on a fault with a similar NNE-SSW orientation. Moreover, most historic events in
450 this region have been previously interpreted as slip on NNE-SSW striking faults.
451 The dominant rupture on WNW-ESE faults thus brings a new perspective on the
452 seismotectonics of the diffuse Indo-Australian plate boundary. This would not be
453 the first time a major intraplate earthquake has ruptured at high angle to the
454 existing fracture zones. The Mw=8.1 1998 Balleny Islands earthquake stands as a
455 good example for this (Hjörleifsdóttir et al., 2009). Satriano et al. (2012),
456 however, proposes a different interpretation involving several sequential NNE-
457 SSW ruptures. Their interpretation does not seem to be compatible with our
458 refined model involving two subevents that have strong directivity toward the
459 WNW. The back-projection results presented by Satriano et al. (2012) are not,
460 however, inconsistent with our results. This is particularly true for their high-
461 resolution image obtained with a passband of 0.5 to 1.0 Hz, which is in very good
462 agreement with our most robust two-point-source model. We do not exclude
463 such complicated models involving (possibly orthogonal) NNE-SSW faults, as
464 long as these ruptures do not violate the constraints from long-period waves (i.e.,
465 scalar seismic moment, surface wave radiation pattern and the overall westward
466 directivity). If more complex rupture models are preferred from other data sets,
467 such as very high-frequency P waves and teleseismic body waves, these models
468 can be tested against the long-period data presented here, especially the surface-
469 wave radiation patterns, shown in Fig. 6c.

470

471 The Mw=8.6 mainshock was followed two hours later by a Mw=8.2 aftershock,
472 which occurred approximately 200 km to the south. To analyze the source of this
473 major aftershock, we subtracted the SEM synthetics for the Mw=8.6 mainshock
474 from the data and used the corresponding residuals as the data vector. This was
475 done to clean up the seismograms from large amplitude disturbances due to the
476 surface-wave arrivals of the Mw=8.6 mainshock. The focal mechanism obtained
477 for the Mw=8.2 aftershock shows a very small non-double-couple component.
478 This result as well as the surface-wave radiation diagram suggest a simpler
479 rupture than the Mw=8.6 mainshock. This is in good agreement with
480 backprojection results that indicates a simple bilateral rupture along a NNE-SSW
481 fault (Meng et al., 2012).

482

483 Our analysis of the surface-wave amplitudes points out a large centroid depth
484 ($h_c \approx 30$ km) both for the Mw=8.6 mainshock and the Mw=8.2 aftershock. This
485 indicates a relatively large depth extent of faulting. If we consider the simple
486 case of uniform slip with depth up to the seafloor, the depth extent of faulting
487 would be as much as 60 km (i.e., $2 \times h_c$, assuming negligible variation of the shear
488 modulus as a function of depth), so that the slip potency above and below the
489 centroid are equal. If the slip linearly decreased with depth, then the depth
490 extent could be as much as 90 km (i.e., $3 \times h_c$). The latter is more consistent with
491 several finite-fault inversion results for the Mw=8.6 mainshock which indicate
492 fairly large slip at shallow depths (Hayes, 2012; Shao et al., 2012; Wei, 2012; Yue
493 et al., 2012). In any case, the Mw=8.6 and Mw=8.2 2012 Sumatra earthquakes

494 most likely involved substantial lithospheric deformation that may eventually
495 lead to the formation of a localized plate boundary.

496

497 **Acknowledgements**

498 We thank Shengji Wei, Don Helmberger, Thorne Lay and two anonymous
499 reviewers for helpful discussions. This work uses Federation of Digital Seismic
500 Networks (FDSN) seismic data and CMT solutions from the Global CMT catalog.
501 The Incorporated Research Institutions for Seismology (IRIS) Data Management
502 System (DMS) was used to access the data. This work made use of the Matplotlib
503 python library and of the Basemap toolkit. Lingsen Meng and Jean-Paul Ampuero
504 were supported by NSF grant EAR-1015704

505

506

507

508

509

510

511

512

513

514

515

516

517

518 **References**

- 519 Ammon, C.J., Velasco, A.A., Lay, T., 2006. Rapid estimation of first-order rupture
520 characteristics for large earthquakes using surface waves: 2004 Sumatra-
521 Andaman earthquake. *Geophys. Res. Lett.* 33, L14314.
- 522 Bassin, C., Laske, G., Masters, G., 2000. The Current Limits of resolution for
523 surface wave tomography in North America. *Eos Trans. AGU* 81.
- 524 Ben-Menahem, A., 1961. Radiation of seismic surface-waves from finite moving
525 sources. *Bulletin of the Seismological Society of*
- 526 Ben-Menahem, A., Aboodi, E., Schild, R., 1974. The source of the great Assam
527 earthquake — an interplate wedge motion. *Phys. Earth Planet. Inter.* 9, 265–
528 289.
- 529 Bertero, M., Bindi, D., Boccacci, P., Cattaneo, M., Eva, C., Lanza, V., 1999.
530 Application of the projected Landweber method to the estimation of the
531 source time function in seismology. *Inverse Problems* 13, 465–486.
- 532 Chen, W., Molnar, P., 1977. Seismic moments of major earthquakes and the
533 average rate of slip in central Asia. *J. Geophys. Res.* 82, 2945–2969.
- 534 Delescluse, M., Chamot-Rooke, N., 2007. Instantaneous deformation and
535 kinematics of the India–Australia Plate. *Geophys. J. R. astr. Soc.* 168, 818–842.
- 536 Demets, C., Gordon, R.G., Argus, D.F., 2010. Geologically current plate motions.
537 *Geophys. J. R. astr. Soc.* 181, 1–80.
- 538 Deplus, C., Diament, M., Hébert, H., Bertrand, G., Dominguez, S., Dubois, J., Malod,
539 J., Patriat, P., Pontoise, B., Sibilla, J.-J., 1998. Direct evidence of active
540 deformation in the eastern Indian oceanic plate. *Geol* 26, 131–134.
- 541 Duputel, Z., Rivera, L., Kanamori, H., Hayes, G., 2012. W phase source inversion
542 for moderate to large earthquakes (1990–2010). *Geophys. J. Int.* 189, 1125–

- 543 1147.
- 544 Duputel, Z., Rivera, L., Kanamori, H., Hayes, G.P., Hirshorn, B., Weinstein, S., 2011.
- 545 Real-time W Phase inversion during the 2011 Off the Pacific Coast of Tohoku
- 546 Earthquake. *Earth Planets Space* 63, 535–539.
- 547 Dziewonski, A.M., Anderson, D.L., 1981. Preliminary reference Earth model. *Phys.*
- 548 *Earth Planet. Inter.* 25, 297–356.
- 549 Haskell, N.A., 1963. Radiation pattern of Rayleigh waves from a fault of arbitrary
- 550 dip and direction of motion in a homogeneous medium. *Bull. seism. Soc. Am.*
- 551 53, 619–642.
- 552 Hauksson, E., Stock, J., Hutton, K., Yang, W., Vidal-Villegas, J.A., Kanamori, H.,
- 553 2010. The 2010 Mw7.2 El Mayor-Cucapah Earthquake Sequence, Baja
- 554 California, Mexico and Southernmost California, USA: Active Seismotectonics
- 555 along the Mexican Pacific Margin. *Pure appl. geophys.* 168, 1255–1277.
- 556 Hayes, G.P., 2012. USGS finite fault model for the Mw=8.6 Earthquake Off the
- 557 West Coast of Northern Sumatra.
- 558 [http://earthquake.usgs.gov/earthquakes/eqinthenews/2012/usc000905e/f
inite_fault.php](http://earthquake.usgs.gov/earthquakes/eqinthenews/2012/usc000905e/finite_fault.php).
- 560 Hayes, G.P., Furlong, K.P., Ammon, C.J., 2009. Intraplate deformation adjacent to
- 561 the Macquarie Ridge south of New Zealand—The tectonic evolution of a
- 562 complex plate boundary. *Tectonophysics* 463, 1–14.
- 563 Hayes, G.P., Rivera, L., Kanamori, H., 2009. Source Inversion of the W-Phase: Real-
- 564 time Implementation and Extension to Low Magnitudes. *Seismol. Res. Lett.*
- 565 80, 817–822.
- 566 Henry, C., Das, S., Woodhouse, J.H., 2000. The great March 25, 1998, Antarctic
- 567 Plate earthquake: Moment tensor and rupture history. *J. Geophys. Res.* 105,

- 568 16097–16118.
- 569 Hjörleifsdóttir, V., Kanamori, H., Tromp, J., 2009. Modeling 3-D wave propagation
570 and finite slip for the 1998 Balleny Islands earthquake. *J. Geophys. Res.*
- 571 Kanamori, H., 1970. Synthesis of long-period surface waves and its application to
572 earthquake source studies—Kurile Islands earthquake of October 13, 1963. *J.*
573 *Geophys. Res.* 75, 5011–5027.
- 574 Kanamori, H., 1993. W phase. *Geophys. Res. Lett.* 20, 1691–1694.
- 575 Kanamori, H., Rivera, L., 2008. Source inversion of W phase: speeding up seismic
576 tsunami warning. *Geophys. J. Int.* 175, 222–238.
- 577 Kiser, E., Ishii, M., 2011. The 2010 Mw 8.8 Chile earthquake: Triggering on
578 multiple segments and frequency-dependent rupture behavior. *Geophys. Res.*
579 *Lett.* 38, L07301.
- 580 Kiser, E., Ishii, M., 2012. Preliminary Rupture Modelling of the April 11, 2012
581 Sumatran Earthquakes.
http://www.seismology.harvard.edu/research_sumatra2012.html.
- 582 Komatitsch, D., Tromp, J., 1999. Introduction to the spectral element method for
583 three-dimensional seismic wave propagation. *Geophys. J. Int.* 139, 806–822.
- 584 Kustowski, B., Ekström, G., Dziewonski, A.M., 2008. Anisotropic shear-wave
585 velocity structure of the Earth’s mantle: A global model. *J. Geophys. Res.* 113,
586 B06306.
- 588 Lanza, V., Spallarossa, D., Cattaneo, M., Bindi, D., Augliera, P., 1999. Source
589 parameters of small events using constrained deconvolution with empirical
590 Green’s functions. *Geophys. J. Int.* 137, 651–662.
- 591 Lay, T., Kanamori, H., Ammon, C.J., Koper, K.D., Hutko, A.R., Ye, L., Yue, H.,
592 Rushing, T.M., 2012. Depth-varying rupture properties of subduction zone

- 593 megathrust faults. *J. Geophys. Res.* 117, B04311.
- 594 Meng, L., Ampuero, J.-P., Stock, J., Duputel, Z., Luo, Y., Tsai, V.C., 2012. An
595 earthquake in a maze: compressional rupture branching in a weakened
596 oceanic lithosphere during the April 11 2012 M8.6 Sumatra earthquake.
- 597 Accepted for publication in *Science*.
- 598 Meng, L., Inbal, A., Ampuero, J.-P., 2011. A window into the complexity of the
599 dynamic rupture of the 2011 Mw 9 Tohoku-Oki earthquake. *Geophys. Res.*
600 Lett. 38, L00G07.
- 601 Okal, E.A., 1977. The July 9 and 23, 1905, Mongolian earthquakes: A surface wave
602 investigation. *Earth Planet Sci. Lett.* 34, 326–331.
- 603 Ruff, L.J., 1984. Tomographic imaging of the earthquake rupture process.
604 *Geophys. Res. Lett.* 11, 629–632.
- 605 Sager, W.W., Paul, C.F., Krishna, K.S., Pringle, M., Eisn, A.E., Frey, F.A., Gopala Rao,
606 D., Levchenko, O., 2010. Large fault fabric of the Ninetyeast Ridge implies
607 near-spreading ridge formation. *Geophys. Res. Lett.* 37, L17304.
- 608 Sambridge, M., 1999. Geophysical inversion with a neighbourhood algorithm-I.
609 Searching a parameter space. *Geophys. J. Int.* 138, 479–494.
- 610 Satriano, C., Kiraly, E., Bernard, P., Villette, J.-P., 2012. The 2012 Mw 8.6 Sumatra
611 earthquake: evidence of westward sequential seismic ruptures associated to
612 the reactivation of a N-S ocean fabric. Accepted for publication in *Geophys.*
613 *Res. Lett.*
- 614 Schlupp, A., Cisternas, A., 2007. Source history of the 1905 great Mongolian
615 earthquakes (Tsetserleg, Bolnay). *Geophys. J. Int.* 169, 1115–1131.
- 616 Shao, G., Li, X., Ji, C., 2012. Preliminary Result of the Apr 11, 2012 Mw 8.64
617 sumatra Earthquake.

- 618 [http://www.geol.ucsb.edu/faculty/ji/big_earthquakes/2012/04/10/sumatr
619 a.html.](http://www.geol.ucsb.edu/faculty/ji/big_earthquakes/2012/04/10/sumatra.html)
- 620 Tocheport, A., Rivera, L., Van der Woerd, J., 2006. A Study of the 14 November
621 2001 Kokoxili Earthquake: History and Geometry of the Rupture from
622 Teleseismic Data and Field Observations. Bull. seism. Soc. Am. 96, 1729–
623 1741.
- 624 Tsai, V.C., Hayes, G.P., Duputel, Z., 2011. Constraints on the long-period moment-
625 dip tradeoff for the Tohoku earthquake. Geophys. Res. Lett. 38, L00G17.
- 626 Tsuboi, S., Komatitsch, D., Ji, C., Tromp, J., 2003. Broadband modeling of the 2002
627 Denali fault earthquake on the Earth Simulator. Phys. Earth Planet. Inter.
628 139, 305–313.
- 629 Wei, S., 2012. Tectonic observatory source Models of Large Earthquakes -
630 April/11/2012 (Mw 8.6), Sumatra.
631 http://www.tectonics.caltech.edu/slip_history/2012_Sumatra/index.html.
- 632 Wiens, D., DeMets, C., Gordon, R., Stein, S., Argus, D., Engeln, J.F., Lundgren, P.,
633 Quible, D., Stein, C., Weinstein, S., Woods, D.F., 1985. A diffuse plate boundary
634 model for Indian Ocean tectonics. Geophys. Res. Lett. 12, 429–432.
- 635 Yue, H., Lay, T., Koper, K.D., 2012. The Great Intraplate Earthquakes of 11 April
636 2012: En Echelon and Conjugate Fault Ruptures on an Emerging Indian-
637 Australian Plate Boundary. Submitted to Nature.
- 638
- 639
- 640
- 641
- 642

643 **Figures**

644

645 **Figure 1: The 2012 Sumatra great earthquake sequence.** **a**, Map of the 2012
646 Sumatra great earthquake region. The 11 April 2012 mainshock can be
647 decomposed into two subevents separated by about 200 km (green mechanisms
648 and circles labeled I and II). The W phase and Global CMT (GCMT) single-point-
649 source solutions for the mainshock (inset green mechanisms), the W phase
650 solutions for the 10 January foreshock (blue mechanism), for the Mw=8.2
651 aftershock (yellow mechanism) and for the 5.8<=Mw<8.2 aftershocks (red
652 mechanisms) are shown. Blue circles indicate the earthquake epicenters and
653 magnitudes from the National Earthquake Information Center (NEIC) catalog
654 between 1 January 1973 and 10 April 2012. Red circles show the events since the
655 Mw=8.6 11 April 2012 earthquake through May 2012. White arrows indicate the
656 direction of motion of the Australian plate relative to the Indian plate at about 13
657 mm/yr (Demets et al., 2010). The red triangles on the globe indicate the
658 locations of broadband stations RER and BFO. **b**, W phase waveforms recorded at
659 station RER (epicentral distance $\Delta=43^\circ$, azimuth $\phi=235^\circ$) and BFO ($\Delta=84^\circ$,
660 $\phi=317^\circ$) during the 11 Mw=8.6 April 2012 Sumatra earthquake. In each figure,
661 the black trace is the vertical broad-band displacement data and the red trace is
662 the very-long-period displacement data filtered in the 200-1000 s passband. The
663 W phase, body wave arrivals (P, PP, S, SS) and the Rayleigh wave train (R) are
664 indicated.

665

666

667

668

669 **Figure 2: Long-period surface-wave directivity for the Mw=8.6 11 April**
670 **2012 Sumatra earthquake and for the Mw=7.3 10 January foreshock.** Ratios
671 between observed and predicted rms amplitudes have been measured in the
672 200-400 s passband. **a** and **b**, Amplitude ratios for the Mw=8.6 mainshock. **c** and
673 **d**, Amplitude ratio measured during the Mw=7.3 foreshock. **a** and **c**, Ratios for
674 Rayleigh R1 and R2 wave trains. **b** and **d**, Ratios for Love G1 and G2 wave trains.
675 Short and long arc wave trains are presented respectively using circles and
676 triangles colored as a function of epicentral distance (Δ). Azimuthal variation of
677 amplitude ratios is larger for Rayleigh waves because of their smaller phase
678 velocity, closer to typical rupture speeds, which enhances their sensitivity to
679 rupture directivity. Inset diagrams are equalized Rayleigh and Love waves in the
680 100-400 s passband.

681

682 **Figure 3: Rayleigh wave MRFs for the Mw=8.6 11 April 2012 Sumatra**
683 **earthquake.** The R1 MRFs obtained using the projected landweber method are
684 ordered as a function of the directivity parameter $\Gamma = \cos(\phi - \phi_r)/c$, where ϕ is
685 the azimuth of the station from the epicenter, ϕ_r is the rupture direction and c is
686 the phase velocity (here we assume $\phi_r = 250^\circ$ and $c=3.8$ km/s). The equivalent
687 azimuth relative to $\phi_r = 250^\circ$ is indicated for groups of stations along the top
688 axis. The positive amplitudes are colored as a function of epicentral distance (Δ).
689 The durations of MRFs systematically increase from 80 s to about 170 s as Γ
690 decreases from left to right. Blue lines I and II identify discrete pulses that are
691 visible on several MRFs.

692

693

694 **Figure 4: Multiple-point-source inversion result for the Mw=8.6 2012**

695 **Sumatra earthquake.** Circles show explored locations in time and space using a

696 modified version of the Neighborhood Algorithm sampler (NA, Sambridge,

697 1999). Their colors indicate the rms misfit normalized by their minimum (i.e.,

698 red-yellow colormap for source I and blue-green colormap for source II). **a**,

699 Explored latitudes and longitudes. Used stations are indicated by blue triangles

700 on the globe. **b**, Explored latitudes and longitudes as a function of explored

701 depths. Explored locations are shown in red for source I (first subevent) and in

702 blue for source II (second subevent). The red and blue stars indicate the

703 corresponding optimum locations. **c**, Explored point-source delays for source II

704 (second subevent) as a function of explored point-source delay for source I (first

705 subevent). The colormap used in **c** corresponds to the colormap of source I in **a**

706 and **b**.

707

708

709 **Figure 5: Waveform fit for single and double-point-source models.** Long-

710 period (150-500 s) surface wave motions at station BRVK, MBAR and TIXI (black

711 traces) are compared to predictions for the Global CMT simple point-source

712 solution (red traces, on left) and for the two subevent model (red traces, on

713 right). The waveform segments used in the multiple point source inversion are

714 bounded by red dots.

715

716 **Figure 6: Comparison of observed and predicted surface-wave radiation**
717 **patterns for three simple rupture models.** Comparison of observed (red
718 circles) and predicted (blue triangles) equalized amplitudes for Rayleigh R1, R2
719 (middle) and Love G1, G2 (right). **a**, Single-point-source model. **b**, Two-point-
720 source model. **c**, Optimum source model assuming uniform slip and horizontal
721 rupture propagation: two parallel WNW-ESE bilateral ruptures with significant
722 directivity in the WNW direction.

723

724

725 **Figure 7: Comparison between observed and predicted long-period**
726 **Rayleigh wave amplitudes for the Mw=8.6 mainshock at different centroid**
727 **depths.** The amplitudes are measured in the 200-600 s passband and predicted
728 amplitudes are computed for the two-point-source model presented in section 5.
729 Black circles and triangles indicate the rms amplitudes measured for R1 and R2,
730 respectively. The corresponding least-square best-fit line is shown in red and the
731 1:1 relationship between data and synthetics is shown with a dashed line.

732

733 **Figure 8: Comparison between observed and predicted long-period**
734 **Rayleigh wave amplitudes for the Mw=8.2 aftershock at different centroid**
735 **depths.** The amplitudes are measured in the 100-400 s passband and predicted
736 amplitudes are computed for the single-point-source model presented in section
737 2. Black circles indicate the rms amplitudes measured at each station. The
738 corresponding least-square best-fit line is shown in red and the 1:1 relationship
739 between data and synthetics is shown with a dashed line.

740

741 **Figure 9: High-frequency observations during the Mw=8.6 2012 Sumatra**
742 **earthquake.** High-frequency source imaging results of the Mw=8.6 Sumatra
743 earthquake were obtained by Meng et al. (2012). **a**, Back-projection results
744 obtained using European networks. **b**, Back-projection results obtained using the
745 Hi-Net Japanese network. Colored circles and squares indicate, respectively, the
746 position of primary and secondary peaks of high-frequency radiation. The two-
747 point-source model obtained in the present study is indicated for comparison
748 (green mechanisms and stars labeled I and II). The upper right inset in **a** shows
749 the interpreted fault planes proposed by Meng et al. (2012). **c**, P wave coda
750 stacks between 30° and 95° of epicentral distance. Only stacks with more than 3
751 traces are depicted. The grey dashed line indicates a discrete phase which is
752 visible at different azimuths approximately 100 s after the P wave arrival.

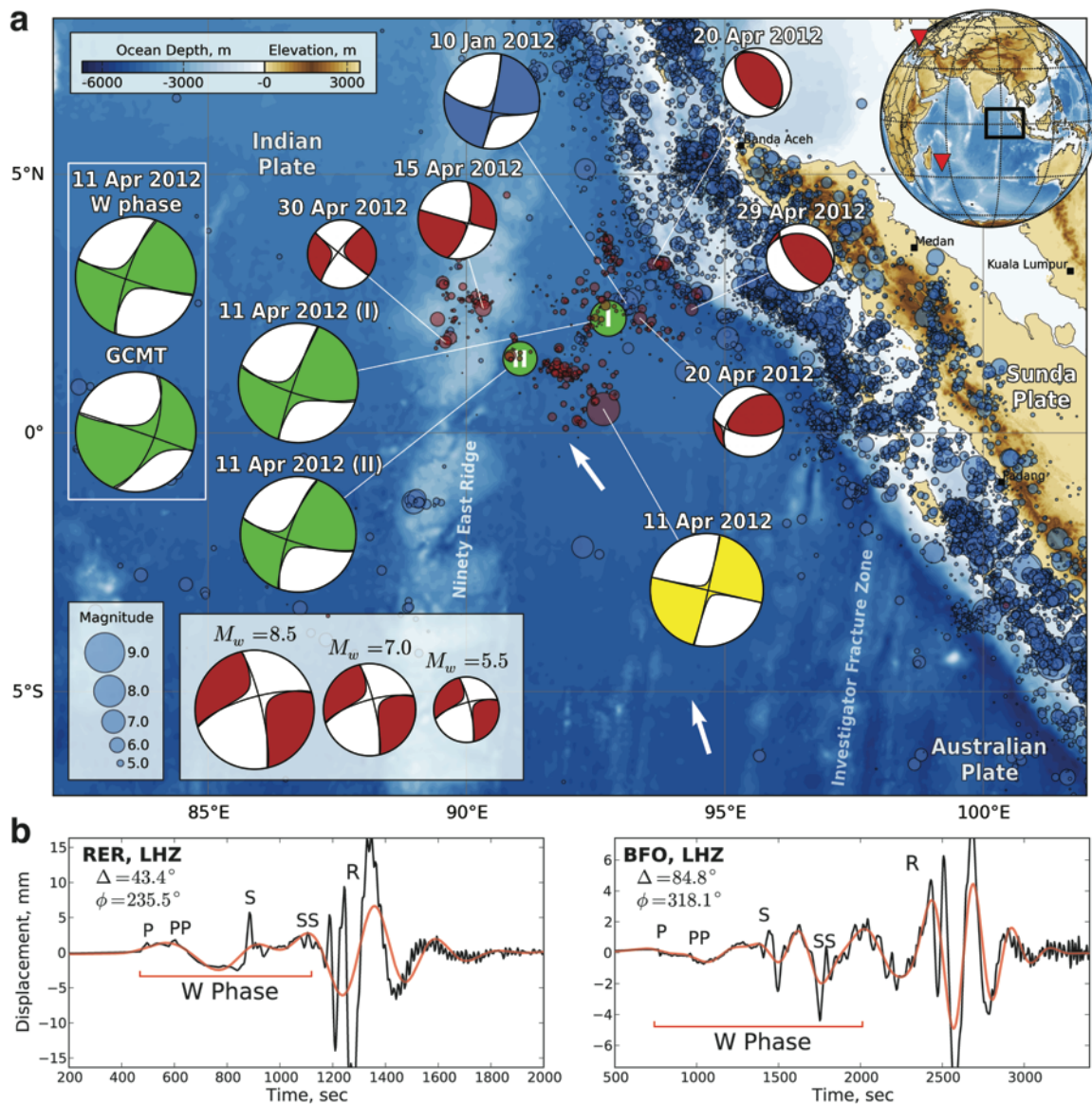


Figure 1

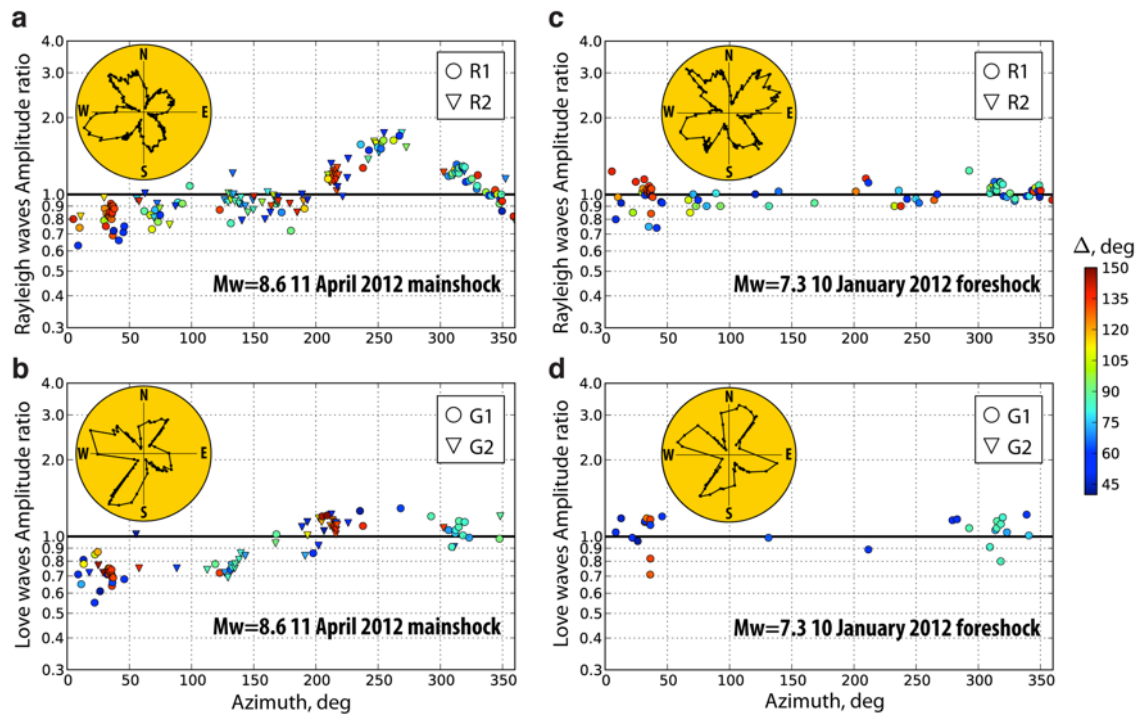


Figure 2

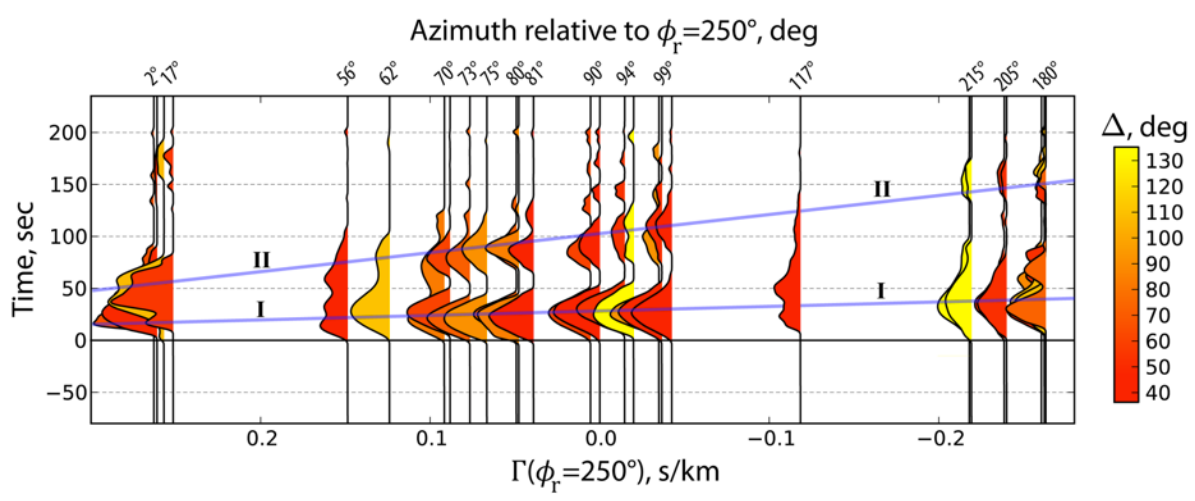


Figure 3

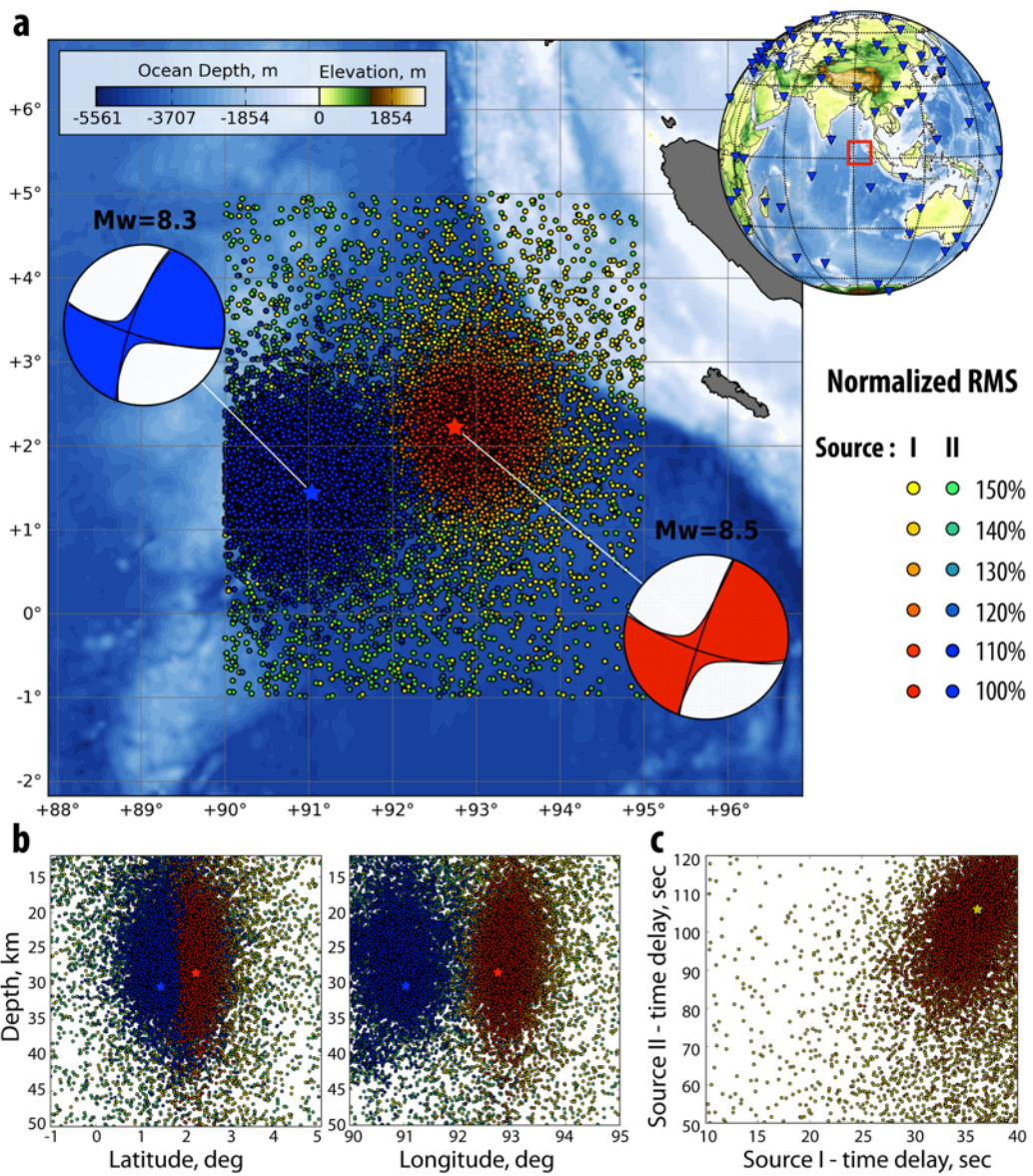


Figure 4

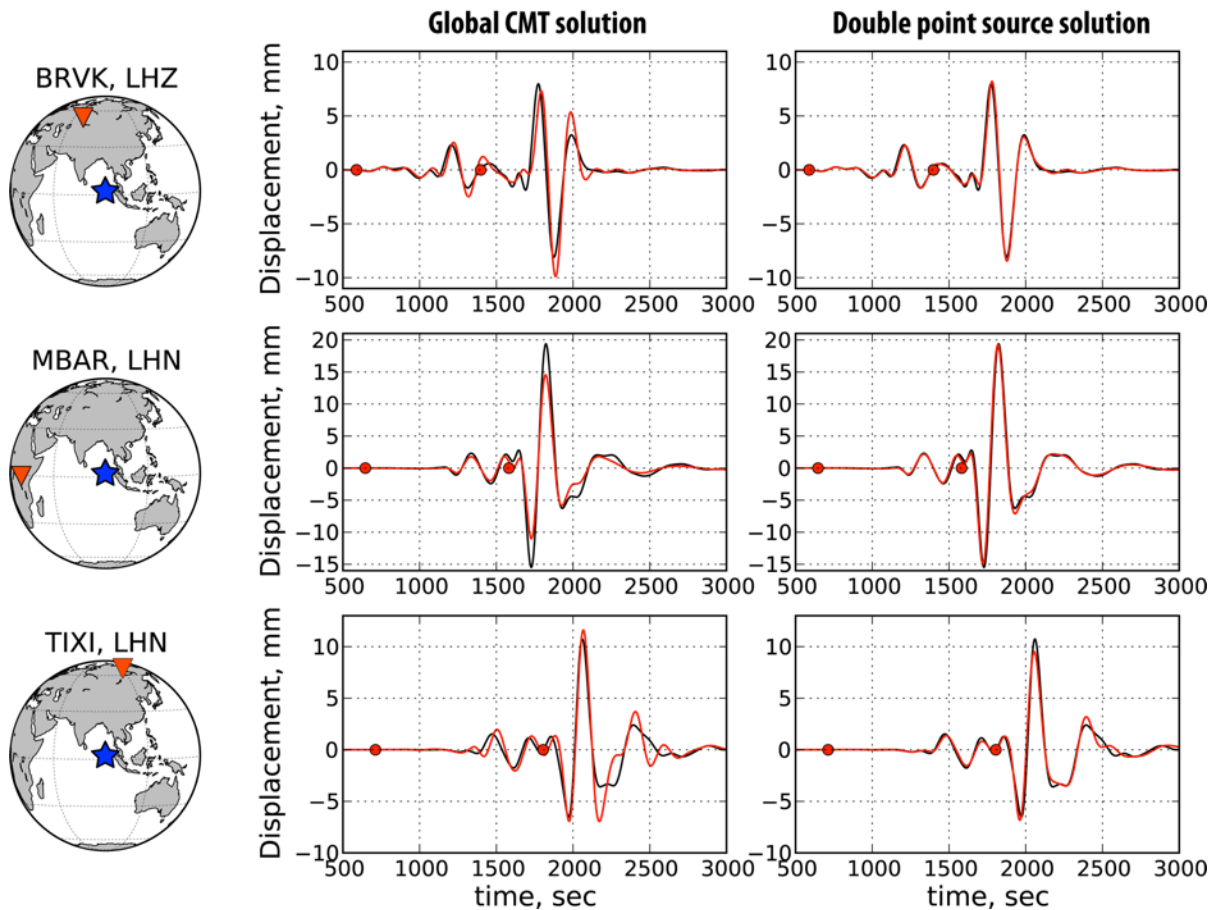


Figure 5

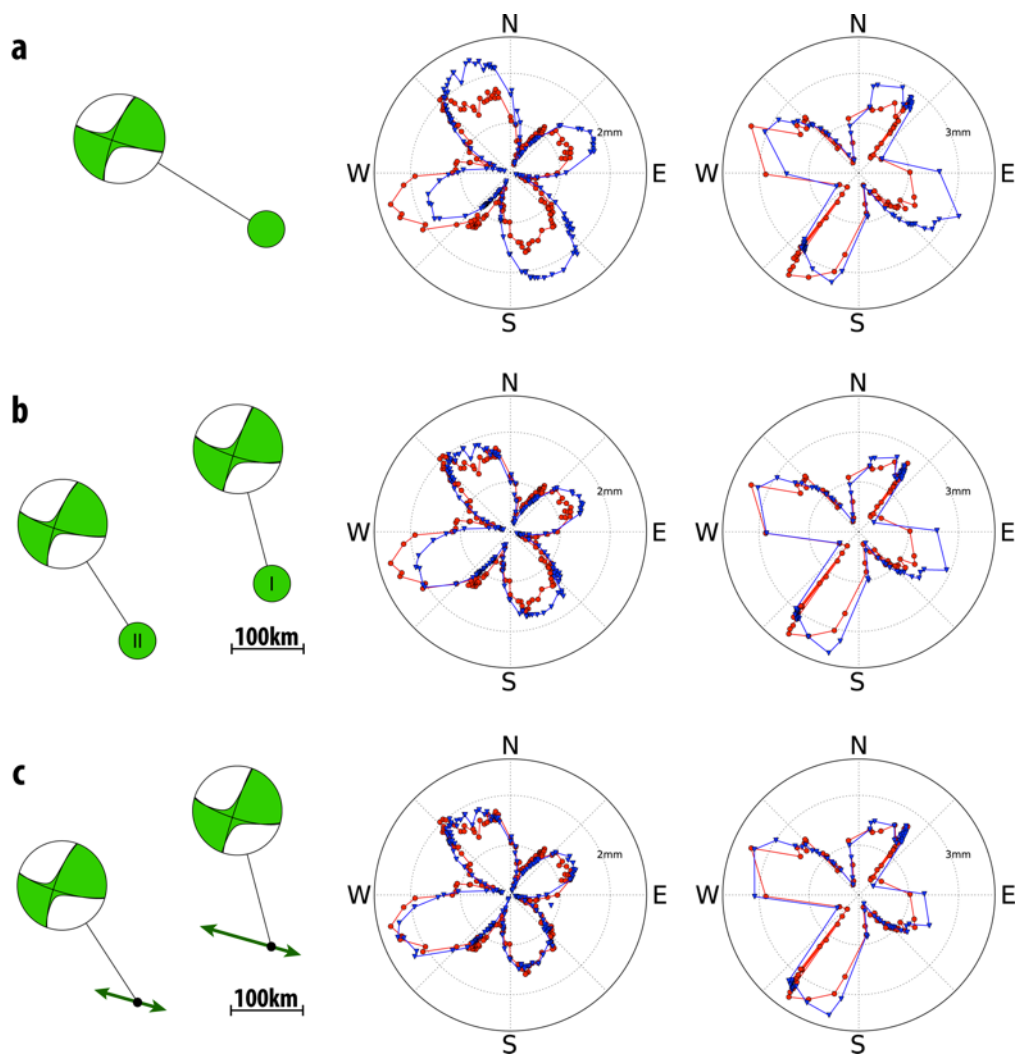


Figure 6

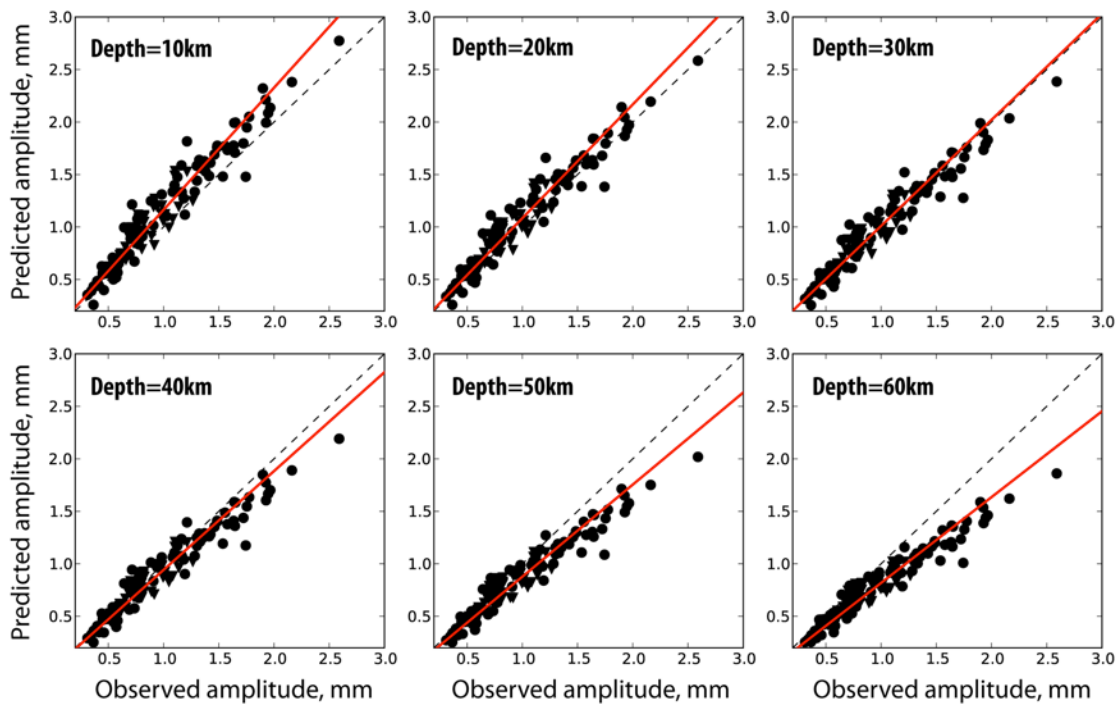


Figure 7

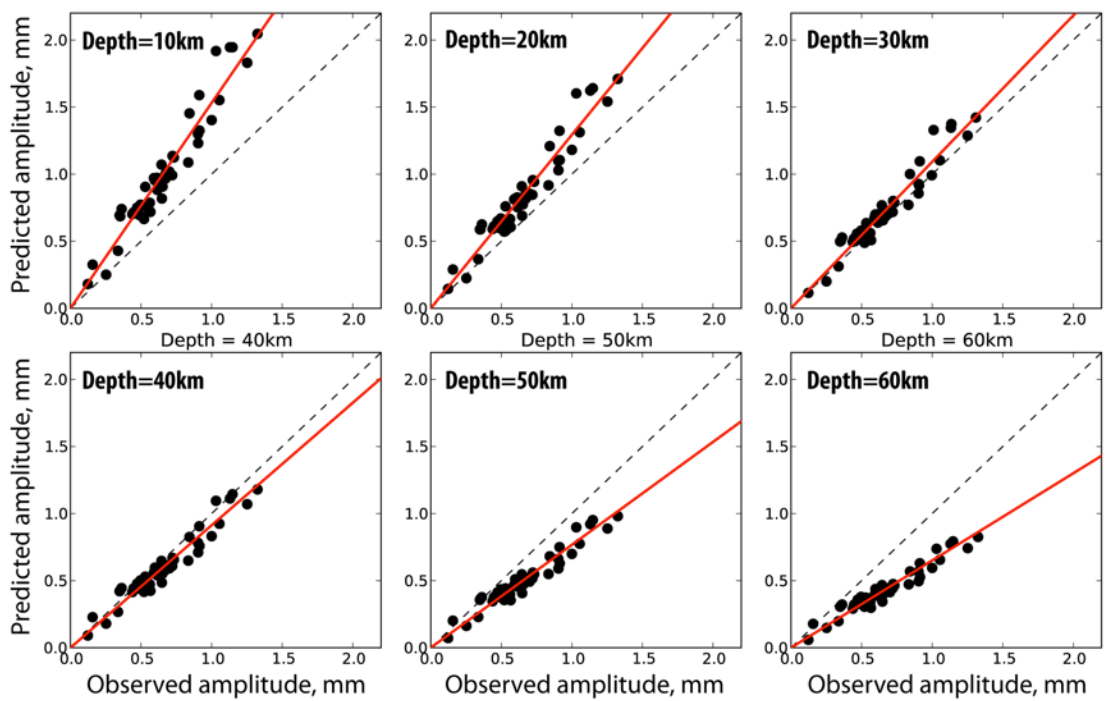


Figure 8

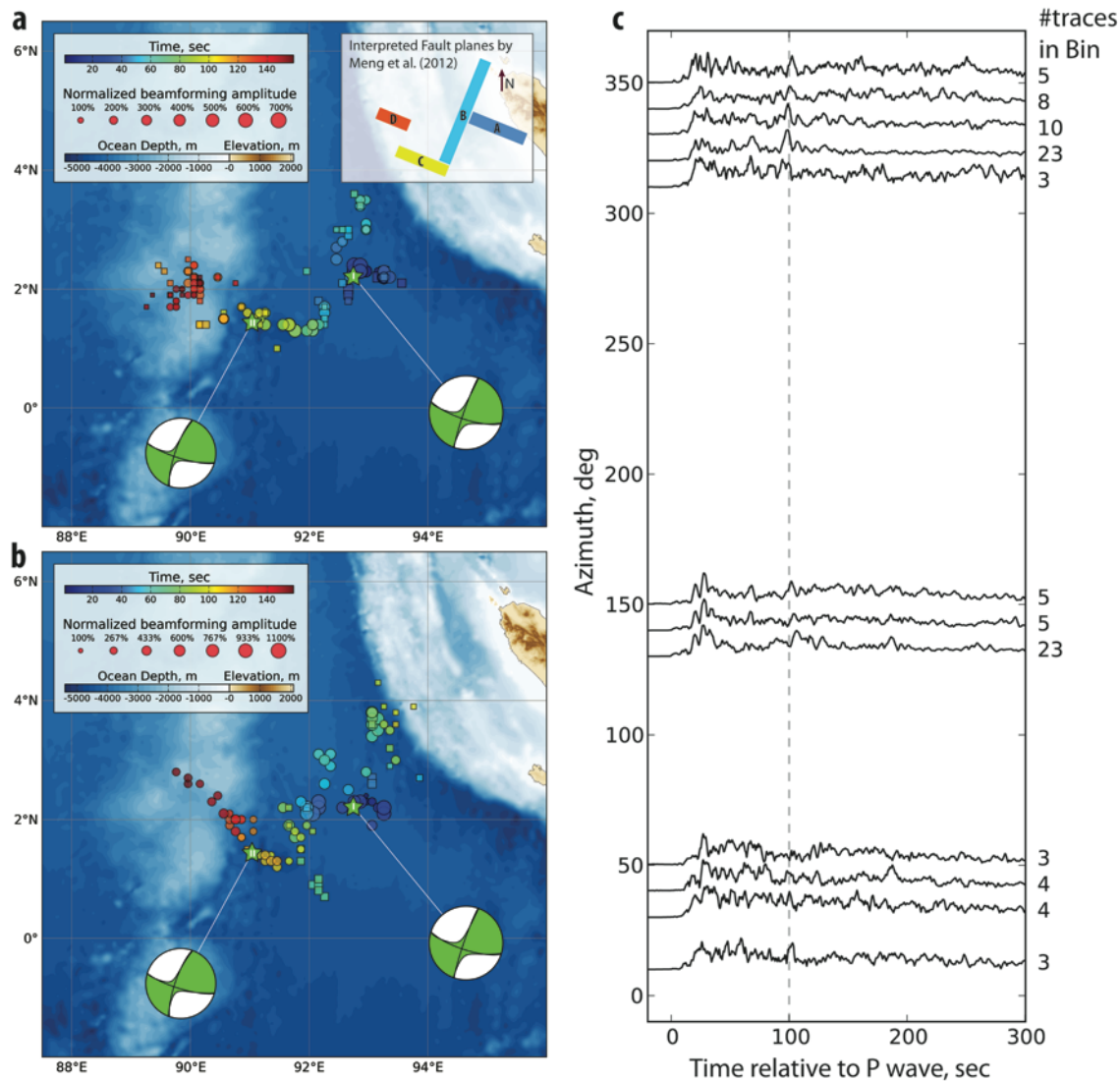


Figure 9

1 **SUPPLEMENTARY MATERIAL**

2

3 **The 2012 Sumatra great earthquake sequence**

4 Zacharie Duputel^{1*}, Hiroo Kanamori¹, Victor C. Tsai¹, Luis Rivera²,

5 Lingsen Meng¹, Jean-Paul Ampuero¹ and Joann M. Stock¹.

6 (1) Seismological Laboratory, California Institute of Technology, 1200E.

7 California Blvd., Pasadena, California 91125, USA.

8 (2) IPGS-EOST, CNRS/Université de Strasbourg, UMR 7516, 5 rue René

9 Descartes, 67084 Strasbourg Cedex, France.

10

11 **Centroid depth**

12 The source excitation kernels of long-period fundamental mode Love waves for a
13 strike-slip source such as the Mw=8.6 Sumatra earthquake do not vary much
14 with depth within the first hundred kilometers (Kanamori and Given, 1981). On
15 the other hand, the corresponding Rayleigh wave kernel values decrease with
16 depth. This is illustrated on Fig. S15b which shows Rayleigh and Love wave
17 seismograms at station AQU computed for two different centroid depths (10 km
18 and 30 km). The Love waveform is very similar for different centroid depths
19 contrarily to Rayleigh waves for which the amplitudes decrease with depth.

20

21 To obtain an estimate of the centroid depth for the Mw=8.6 mainshock, we
22 compare directly the observed and predicted Rayleigh wave / Love wave
23 amplitude ratios (R/L ratios) at different depths. The depths estimated at
24 individual stations are presented on the histogram in Fig. S15a. We also

25 measured an average R/L ratio after amplitude equalization to $\Delta=90^\circ$ (using the
26 procedure of Kanamori, 1970) and azimuthal correction due to the mechanism.
27 The comparison of the average observed and predicted R/L ratios is shown on
28 Fig. S15a, for 3 different source models: Global CMT, W phase single-point-
29 source solution and the double-point-source model presented in section 5 of the
30 main text. This first order depth estimation clearly excludes the possibility of a
31 very shallow centroid depth and suggests an optimum depth around 30 km.
32 Another way of estimating the centroid depth is to focus on the Rayleigh waves
33 only and to compare the observed and predicted amplitudes at different depths
34 for different source models. SEM synthetics were computed for a 3D earth
35 (S362ANI and Crust2.0), for various depths between 10 km and 60 km. The
36 optimum depth can then be defined as the one showing observed/predicted
37 amplitude ratios closest to unity. Fig. S16 shows the amplitude ratios computed
38 for the Global CMT and for the two-point-source model presented in section 5.
39 Although the effect of source directivity makes this plot difficult to interpret, it
40 seems that the optimum source depth ranges between 20 km and 40 km. This is
41 clearly confirmed by the direct comparison between observed and predicted
42 amplitudes shown on Fig. 7 of the main text that indicates an optimum centroid
43 depth around 30 km.

44

45

46

47

48

49

50 **References**

51 Kanamori, H., 1970. Synthesis of long-period surface waves and its application to
52 earthquake source studies—Kurile Islands earthquake of October 13, 1963. *J.*

53 *Geophys. Res.* 75, 5011–5027.

54 Kanamori, H., Given, J.W., 1981. Use of long-period surface waves for rapid
55 determination of earthquake-source parameters. *Phys. Earth Planet. Inter.*
56 27, 8–31.

57

58

59

60

61

62

63

64

65

66

67

68

69

70

71

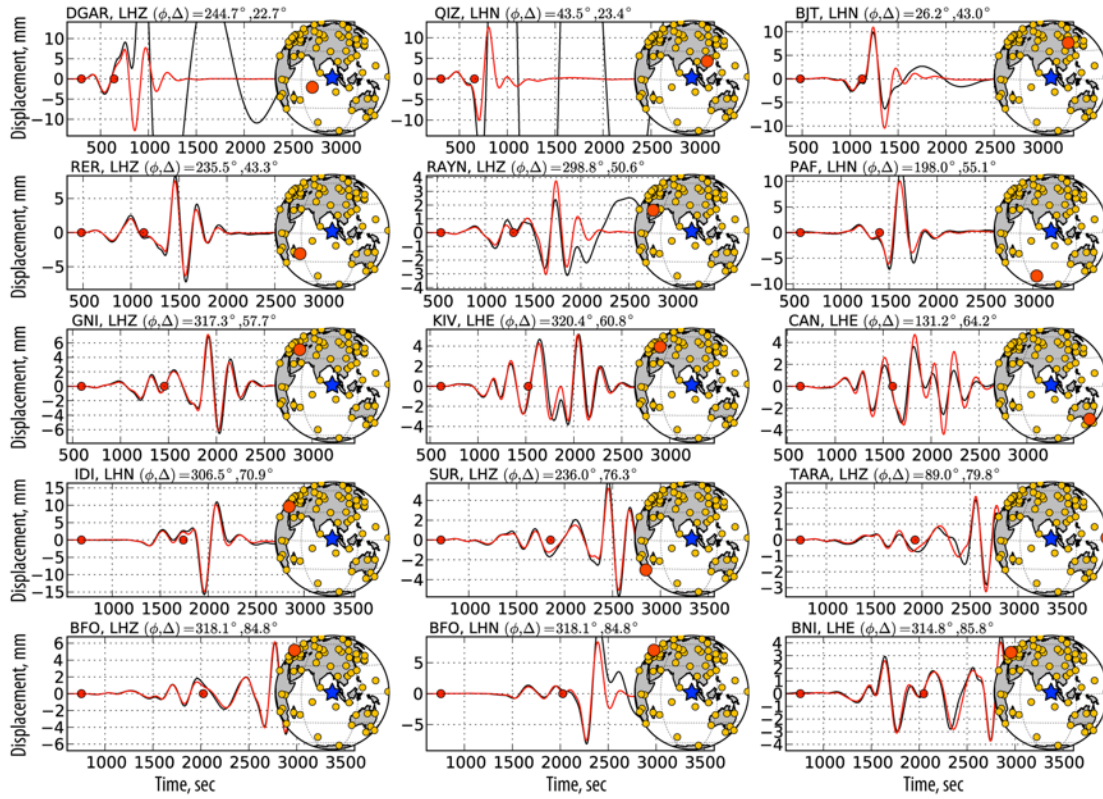
72

73

74

75 **Supplementary Figures**

76



77

78 **Figure S1: W phase waveform comparison for the Mw=8.6 2012 Sumatra**

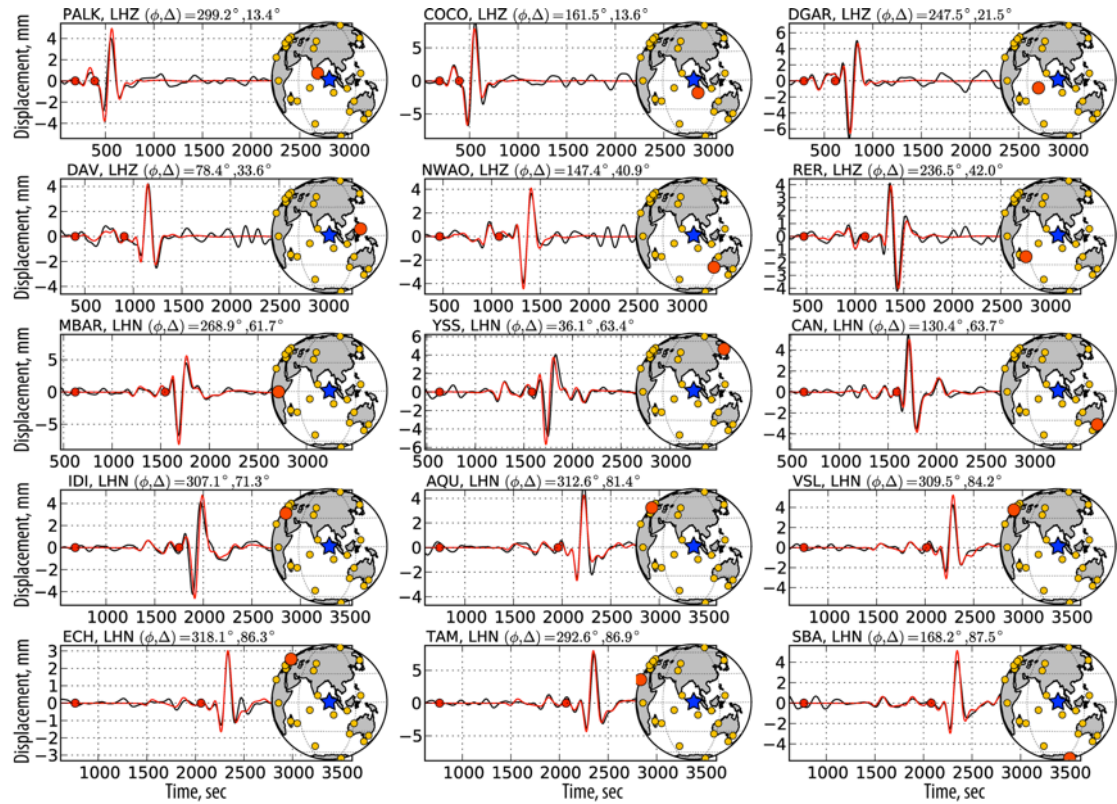
79 **earthquake.** Examples of observed waveforms (black lines) and the
80 corresponding synthetics (red lines) computed from the point-source W phase
81 solution are presented. The station azimuth (ϕ) and epicentral distance (Δ) are
82 indicated, as well as the W phase time window, bounded by red dots. W phase
83 and later arrivals are generally well predicted at very long period. For some
84 channels like DGAR-LHZ, QIZ-LHN, BJT-LHN or RAYN-LHZ, the surface waves are
85 affected by instrument problems (i.e., clipping), though the W phase signal is not
86 affected.

87

88

89

90



91

92 **Figure S2: W phase waveform comparison for the Mw=8.2 2012 Sumatra
93 aftershock.** Examples of residual traces obtained by subtracting double-point-
94 source SEM synthetic seismograms for the Mw=8.6 mainshock from the data
95 (black lines) and the corresponding synthetic seismograms for the Mw=8.2
96 aftershock (red lines) are shown. The station azimuth (ϕ) and epicentral
97 distance (Δ) are indicated, as well as the W phase time window, bounded by red
98 dots. Large amplitude surface waves emerging after the W phase (i.e.,
99 fundamental Rayleigh and Love waves) are generally very well predicted by the
100 W phase solution, even though they are not included in the inversion.

101

102

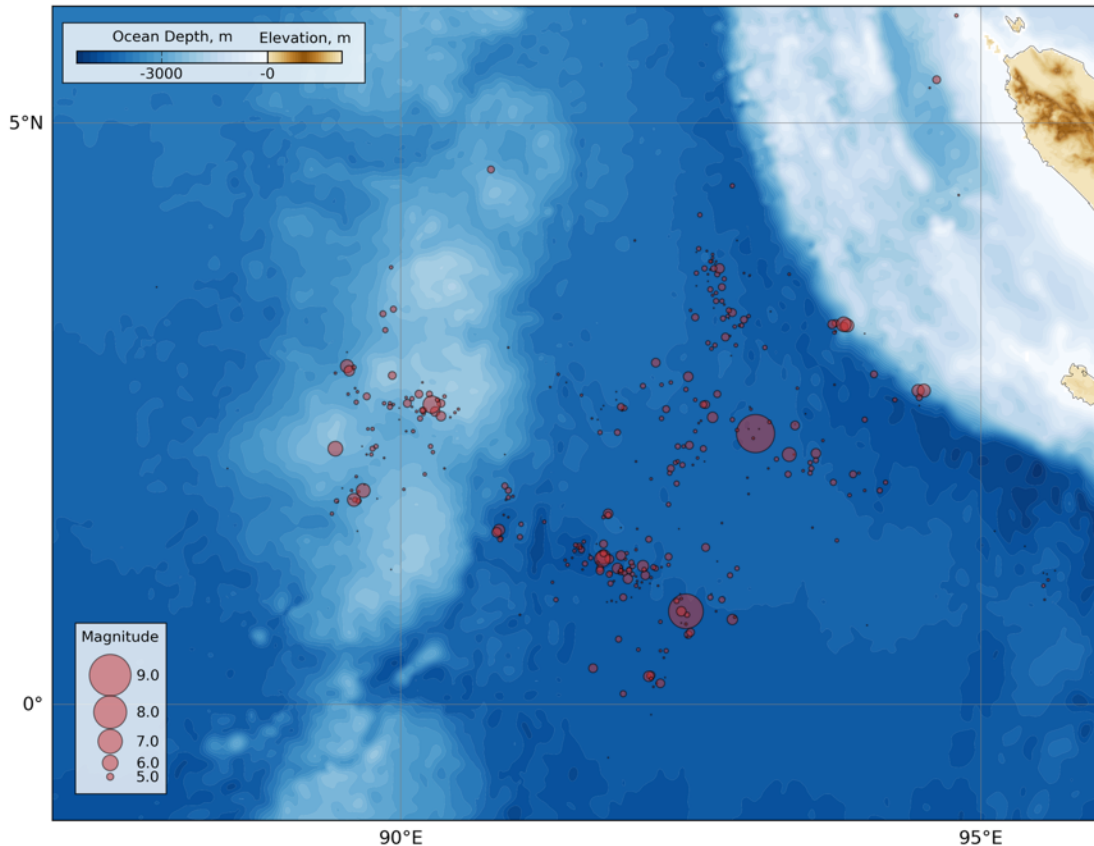
103

104

105

106

107



108

109 **Figure S3: Distribution of the mainshock and aftershocks during the 2012
110 Sumatra earthquake sequence.** The earthquakes hypocenter location from the
111 NEIC catalog between 11 April 2012 and 3 May 2012 are depicted as circles. The
112 circles radius scales linearly with the earthquake magnitude.

113

114

115

116

117

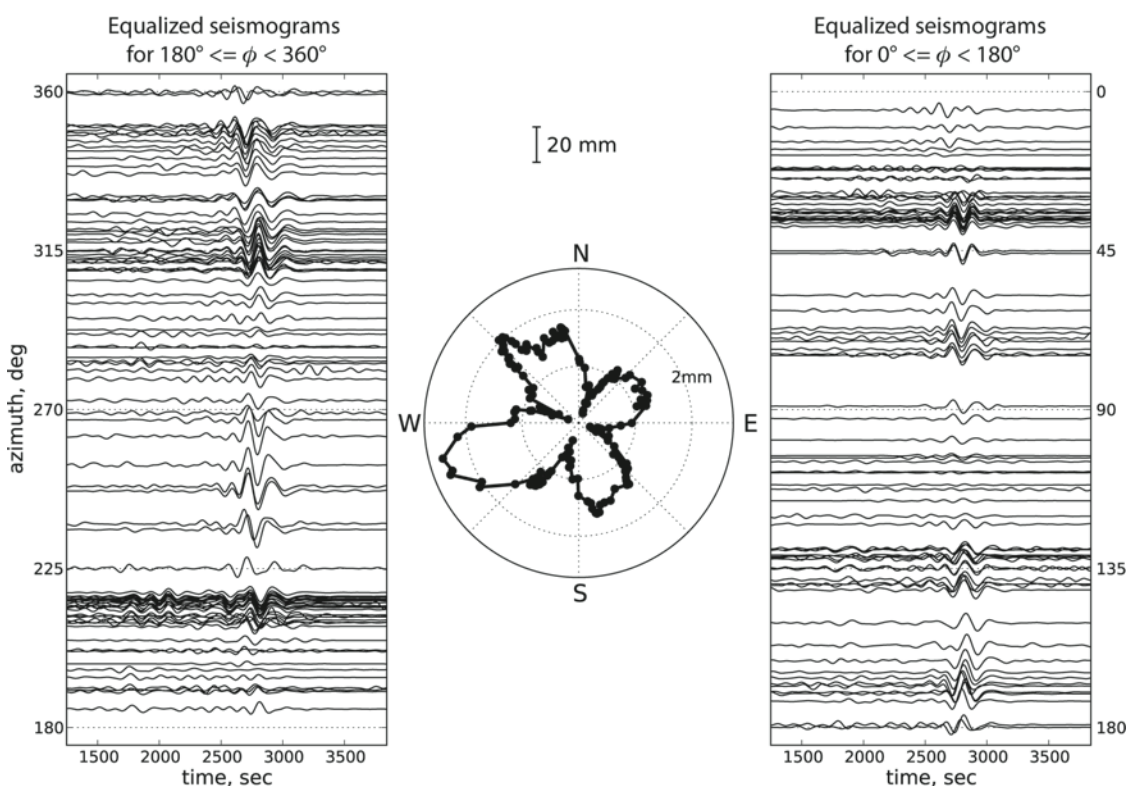
118

119

120

121

122



123

124 **Figure S4: Equalized Rayleigh waves (R1 and R2) for the Mw=8.6 2012**

125 **Sumatra earthquake.** All the seismograms are equalized to a distance of $\Delta_0=90^\circ$.

126 The vertical scale gives the trace amplitude in the 100-400 s passband. The

127 equalized seismograms are ordered as a function of the station azimuth at the

128 source (ϕ).

129

130

131

132

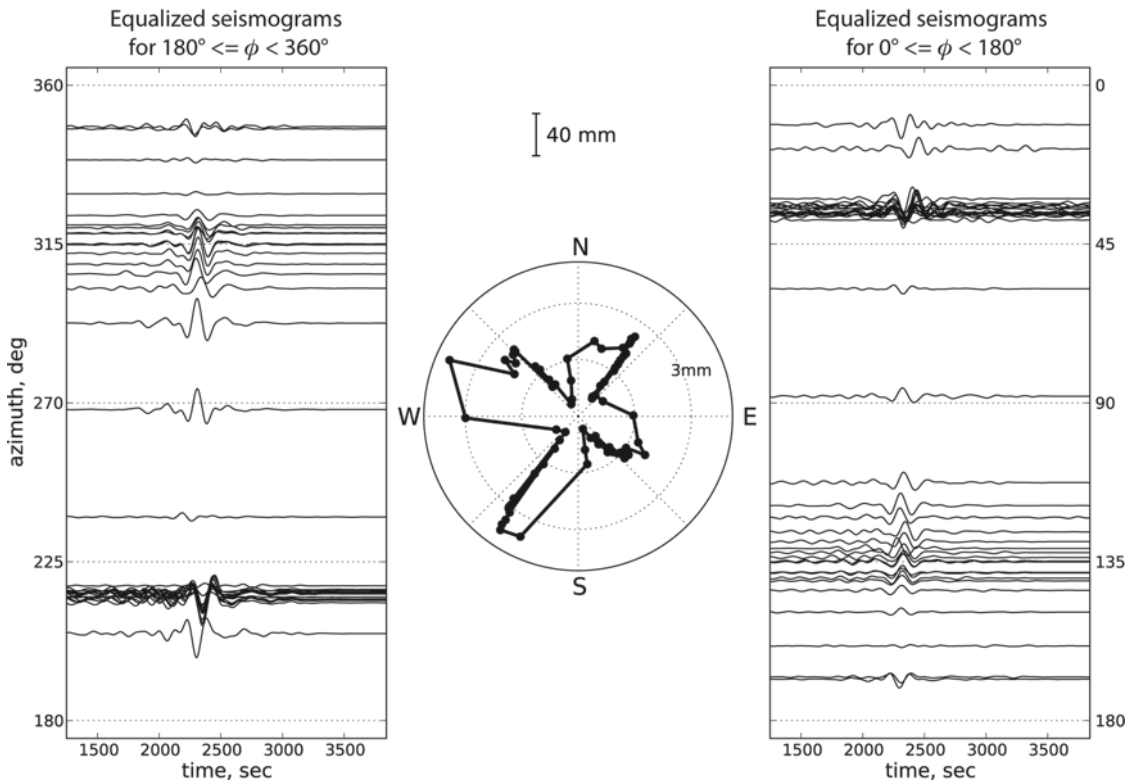
133

134

135

136

137



138

139 **Figure S5: Equalized Love waves (L1 and L2) for the Mw=8.6 2012 Sumatra
140 earthquake.** All the seismograms are equalized to a distance of $\Delta_0=90^\circ$. The
141 vertical scale gives the trace amplitude in the 100-400 s passband. The equalized
142 seismograms are ordered as a function of the station azimuth at the source (ϕ).
143

144

145

146

147

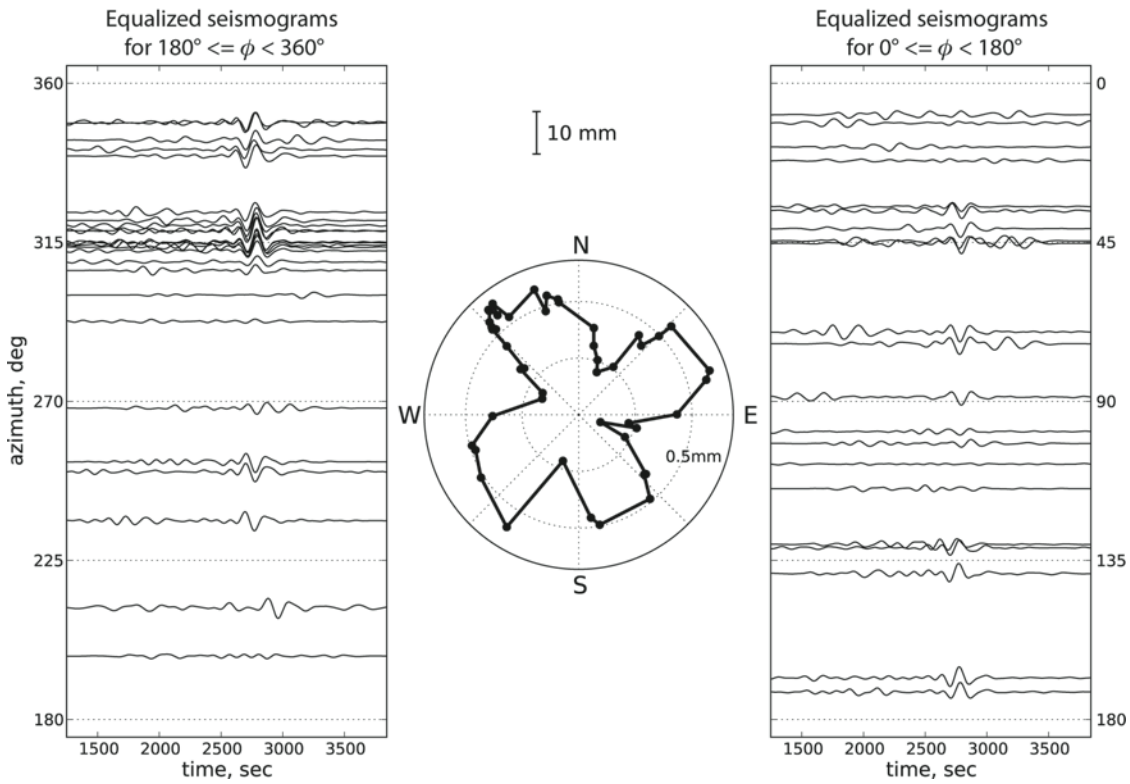
148

149

150

151

152



153

154 **Figure S6: Equalized Rayleigh waves (R1 and R2) for the Mw=8.2 2012**

155 **Sumatra earthquake.** All the seismograms are equalized to a distance of $\Delta_0=90^\circ$.

156 The vertical scale gives the trace amplitude in the 100-400 s passband. The

157 equalized seismograms are ordered as a function of the station azimuth at the

158 source (ϕ).

159

160

161

162

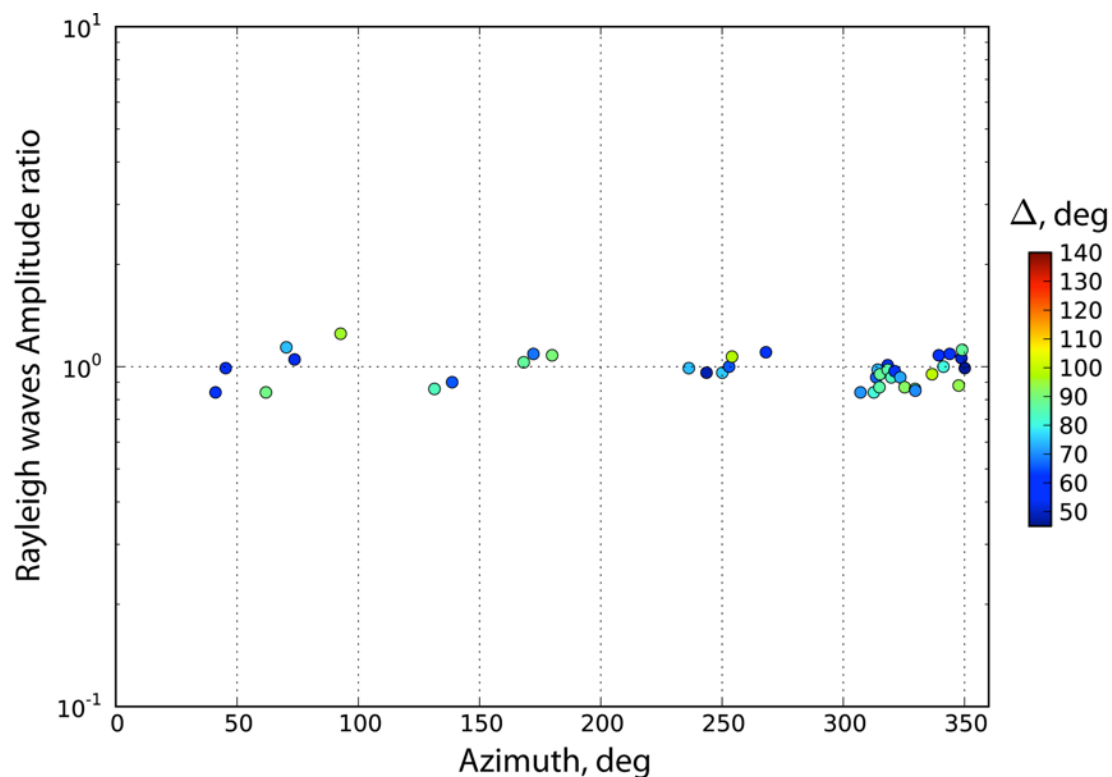
163

164

165

166

167



168

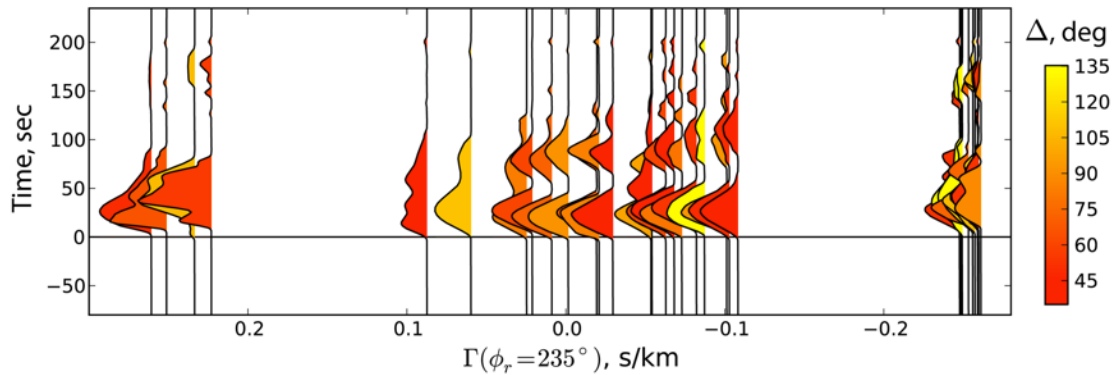
169 **Figure S7: Long-period surface-wave directivity for the Mw=8.2 11 April
170 2012 Sumatra earthquake.** Ratios between observed and predicted rms
171 amplitudes measured in the 100-400 s passband are presented as circles. The
172 circles are colored as a function of epicentral distance (Δ).

173

174

175

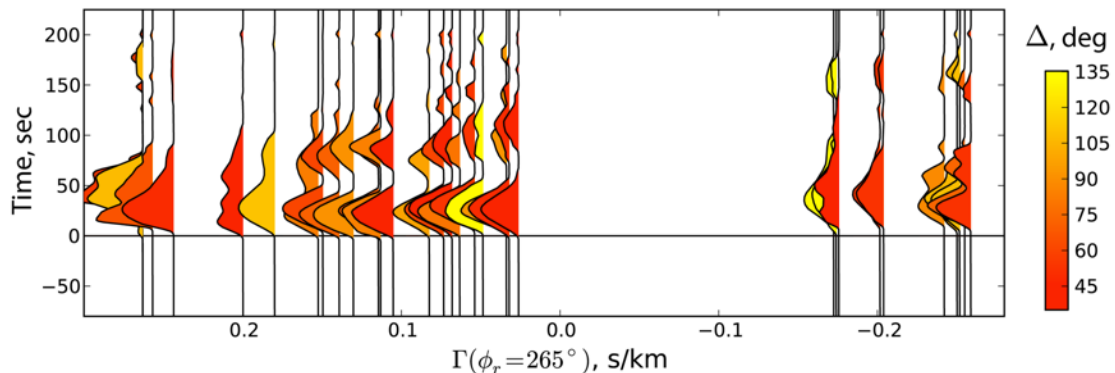
176



177

178 **Figure S8: Rayleigh wave MRFs for the Mw=8.6 11 April 2012 Sumatra**
 179 **earthquake ordered assuming a rupture direction $\phi_r = 235^\circ$.** The R1 MRFs
 180 obtained using the projected landweber method are ordered as a function of the
 181 directivity parameter $\Gamma = \cos(\phi - \phi_r)/c$, where ϕ is the azimuth of the station
 182 from the epicenter, ϕ_r is the rupture direction and c is the phase velocity (here
 183 we assume $\phi_r = 235^\circ$ and $c = 3.8$ km/s).

184



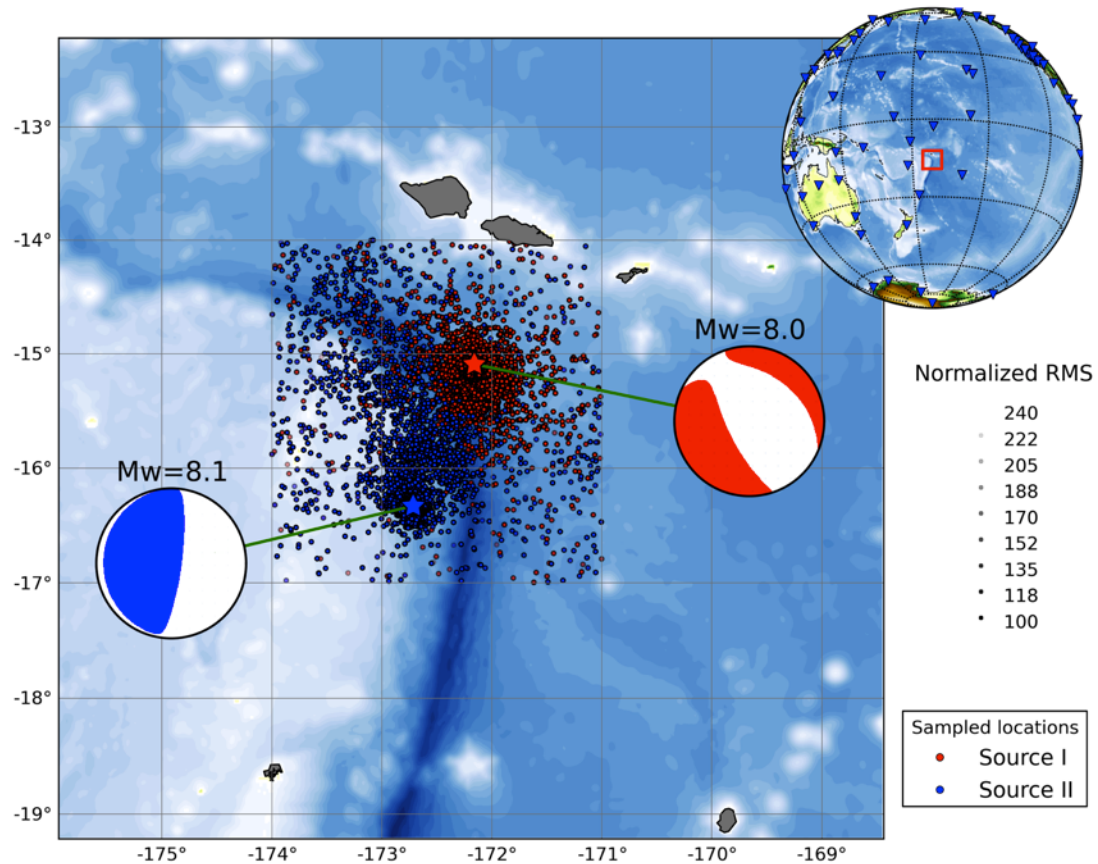
185

186 **Figure S9: Rayleigh wave MRFs for the Mw=8.6 11 April 2012 Sumatra**
 187 **earthquake ordered assuming a rupture direction $\phi_r = 265^\circ$.** The R1 MRFs
 188 obtained using the projected landweber method are ordered as a function of the
 189 directivity parameter $\Gamma = \cos(\phi - \phi_r)/c$, where ϕ is the azimuth of the station
 190 from the epicenter, ϕ_r is the rupture direction and c is the phase velocity (here
 191 we assume $\phi_r = 265^\circ$ and $c = 3.8$ km/s).

192

193

194



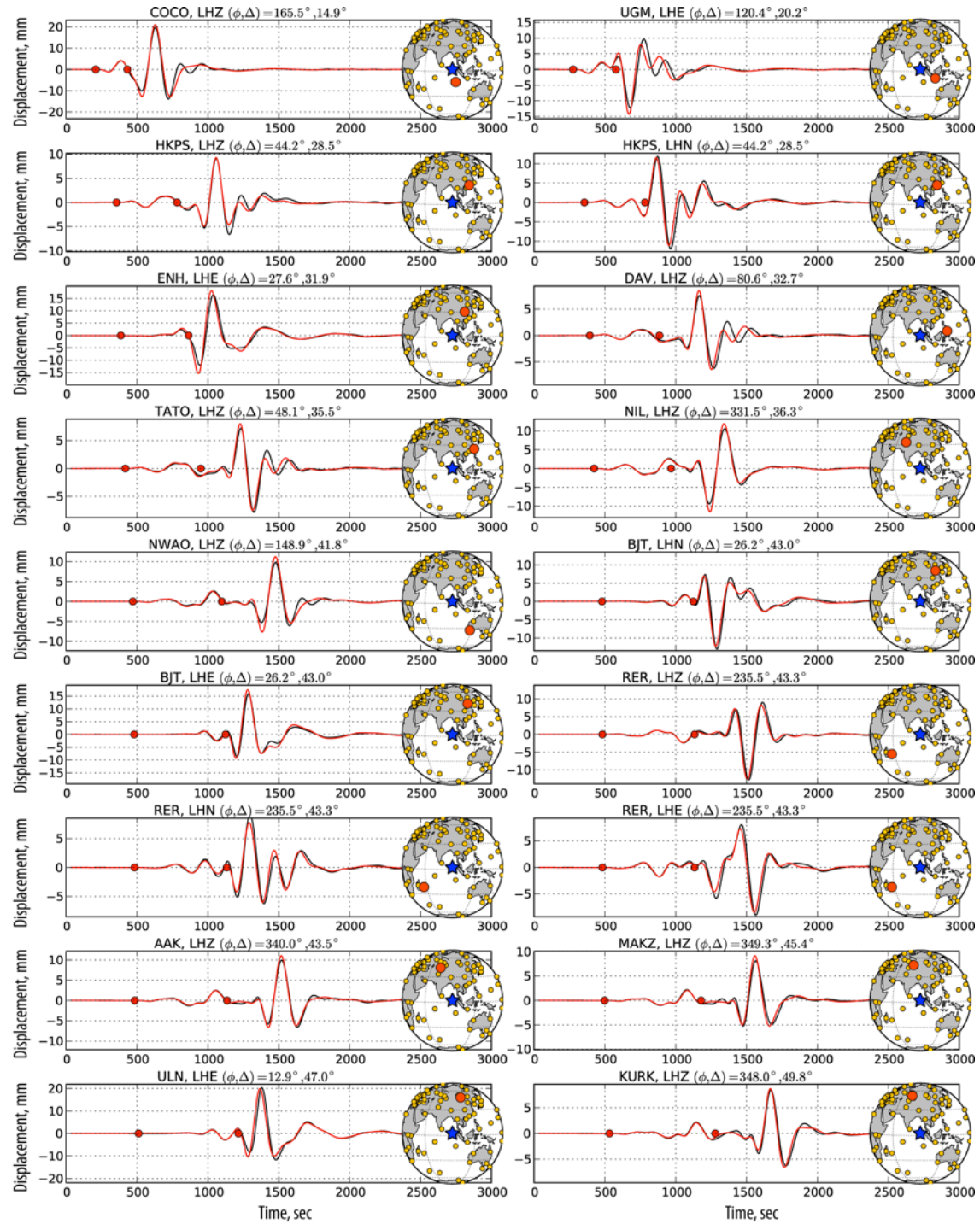
195

196 **Figure S10: Example of multiple-point-source inversion result for the**
197 **Mw=8.1 2009 Samoa earthquake.** Explored latitude and longitude are shown
198 in red for source I (first subevent) and in blue for source II (second subevent).
199 Transparency indicates the rms misfit normalized by its minimum (in percent).
200 Higher sampling is performed in regions associated with smaller rms misfits. The
201 red and blue stars indicate respectively the optimum locations for source I and II.

202

203

204

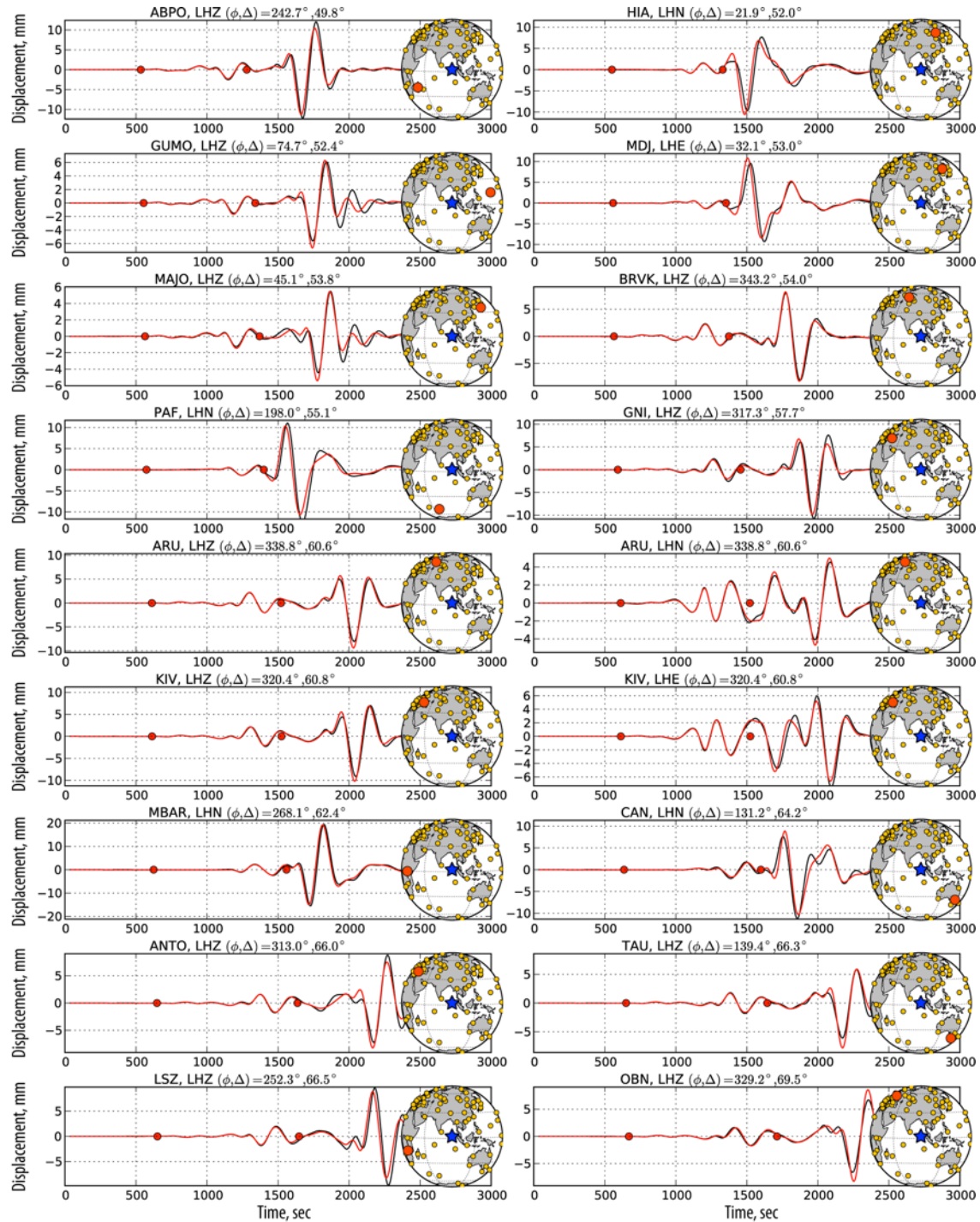


205

206 **Figure S11: Waveform fits for the double-point-source model.** Examples of
 207 observed waveforms (black lines) and the corresponding synthetics (red lines)
 208 computed from the two-point-source model solution are presented. The station
 209 azimuth (ϕ) and epicentral distance (Δ) are indicated, as well as the W phase
 210 time window, bounded by red dots.

211

212



213

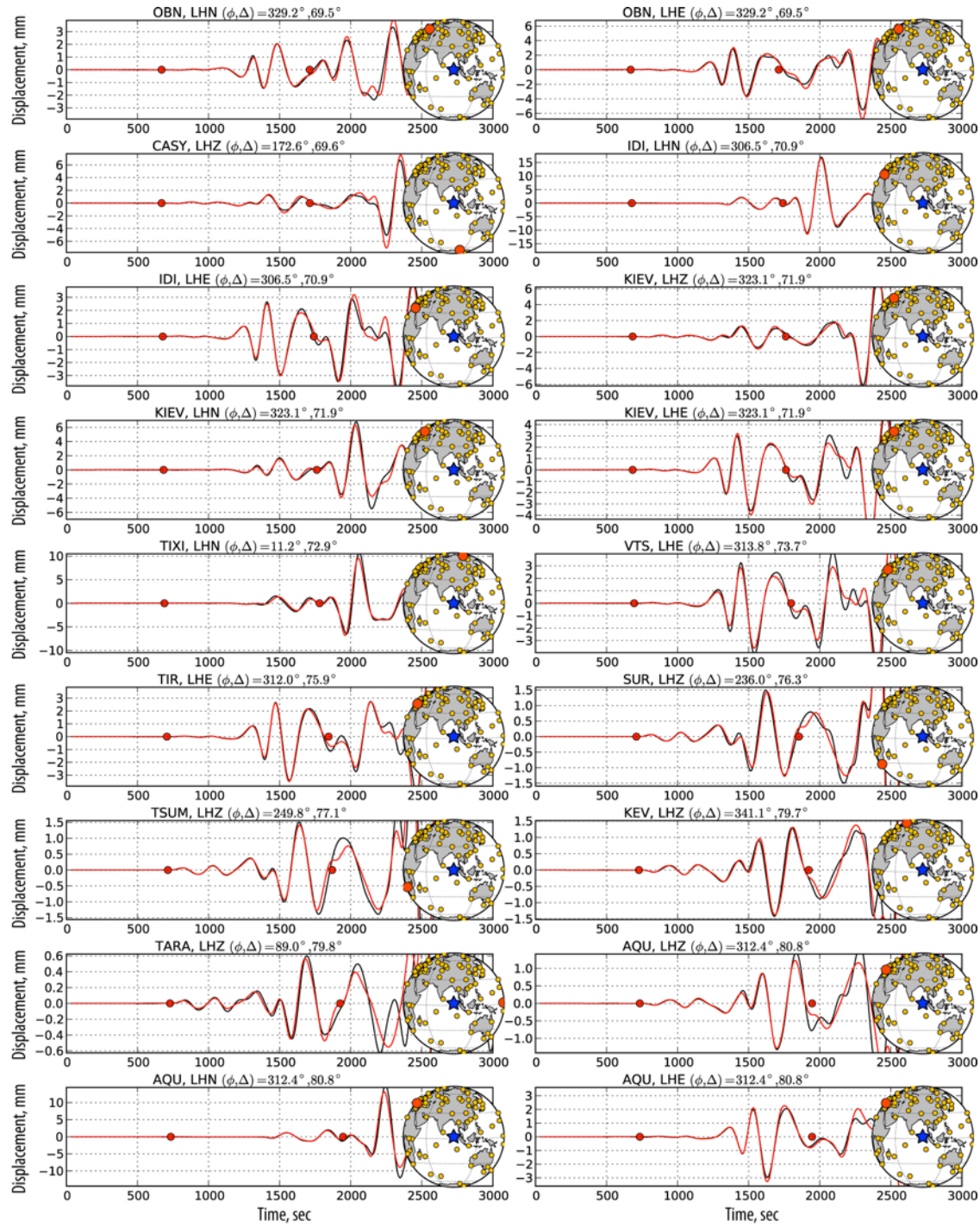
214 **Figure S12:** As in Fig S11.

215

216

217

218



219

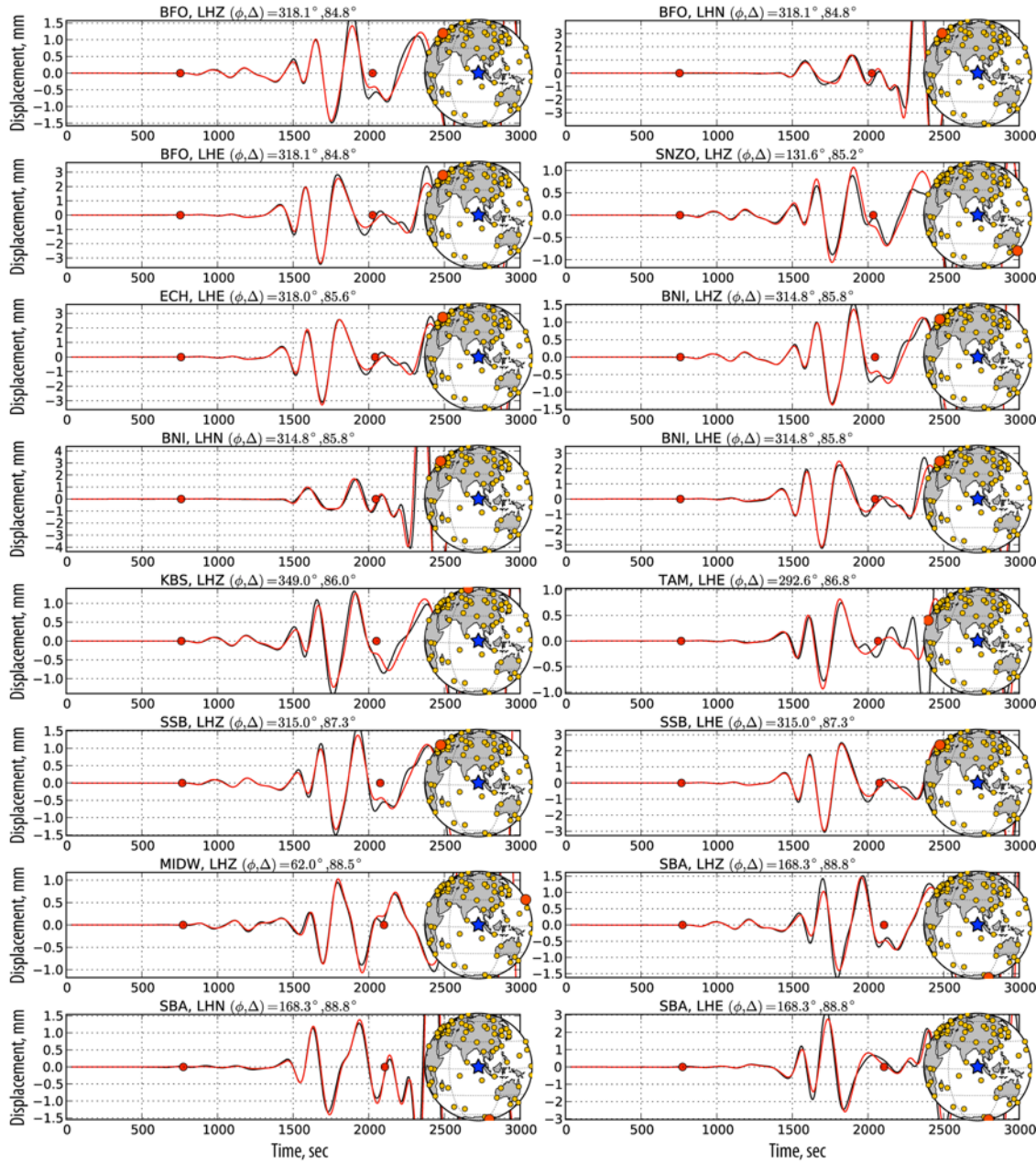
220 **Figure S13:** As in Fig S11.

221

222

223

224



225

226 **Figure S14:** As in Fig S11.

227

228

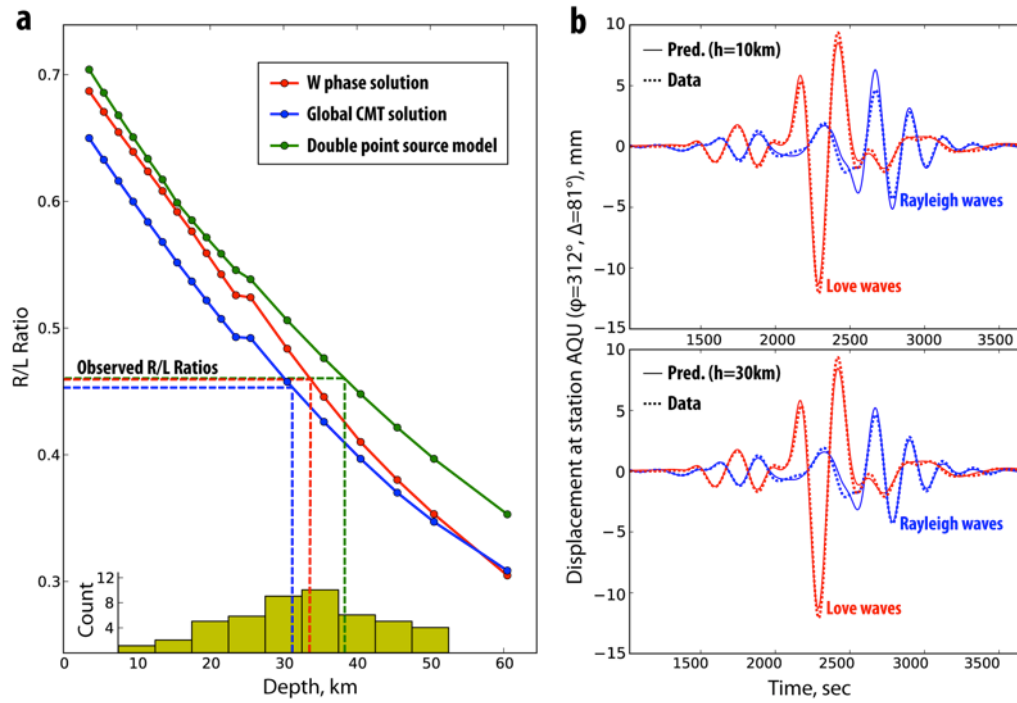
229

230

231

232

233



234

235 **Figure S15: Variation of Rayleigh-wave and Love-wave amplitudes as a**
236 **function of depth. a.** Rayleigh/Love wave amplitude ratios. The observed
237 average amplitude ratios (dashed lines) are compared with the predicted
238 average amplitude ratios computed at different depths for different source
239 models (continuous lines). The depths estimated at individual stations are
240 summarized on the histogram at the bottom. **b.** Observed and predicted
241 waveforms for the two-point-source model at centroid depths of 10km and
242 30km.

243

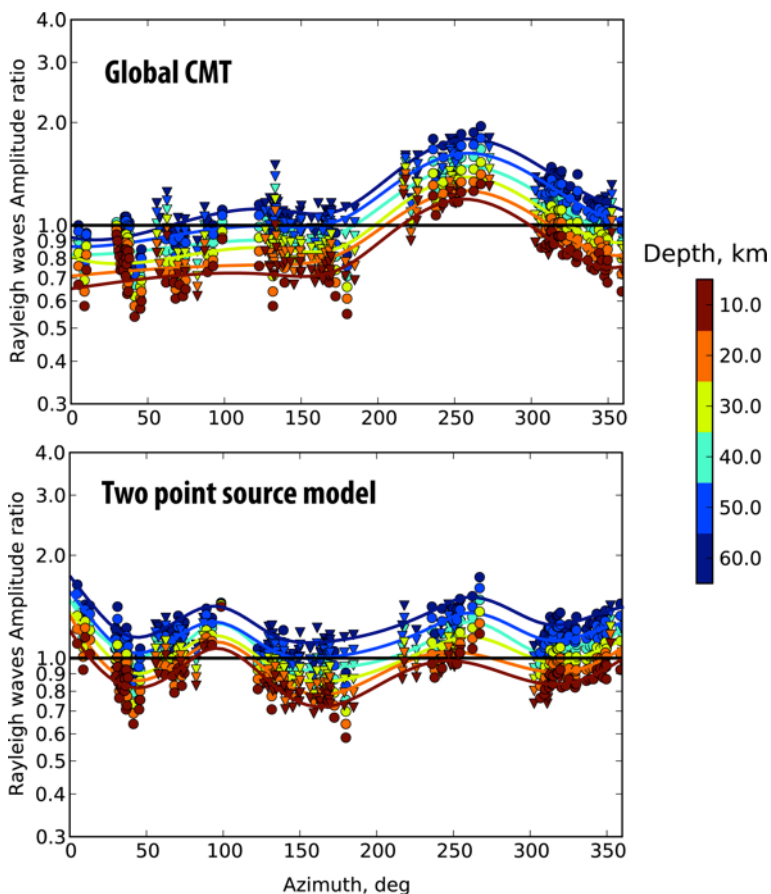
244

245

246

247

248



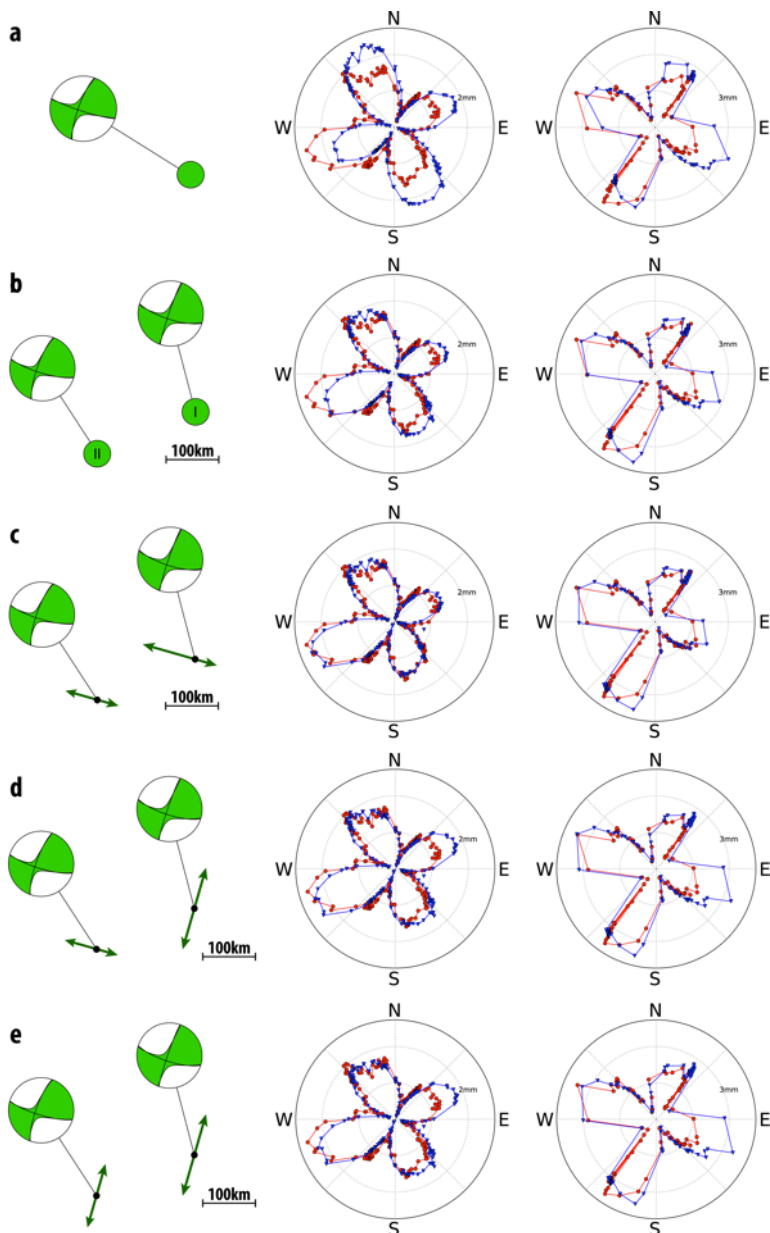
249

250 **Figure S16: Long-period Rayleigh-wave amplitude variation with depth.**

251 Observed / predicted amplitude ratios have been measured in the 200s-600s
252 passband assuming the Global CMT and the two-point-source models. R1 and R2
253 Rayleigh wave trains are presented respectively using circles and triangles. The
254 amplitude ratios have been computed assuming different centroid depths
255 indicated by the colors. Colored lines are smoothed amplitude ratio
256 measurements for each depth.

257

258



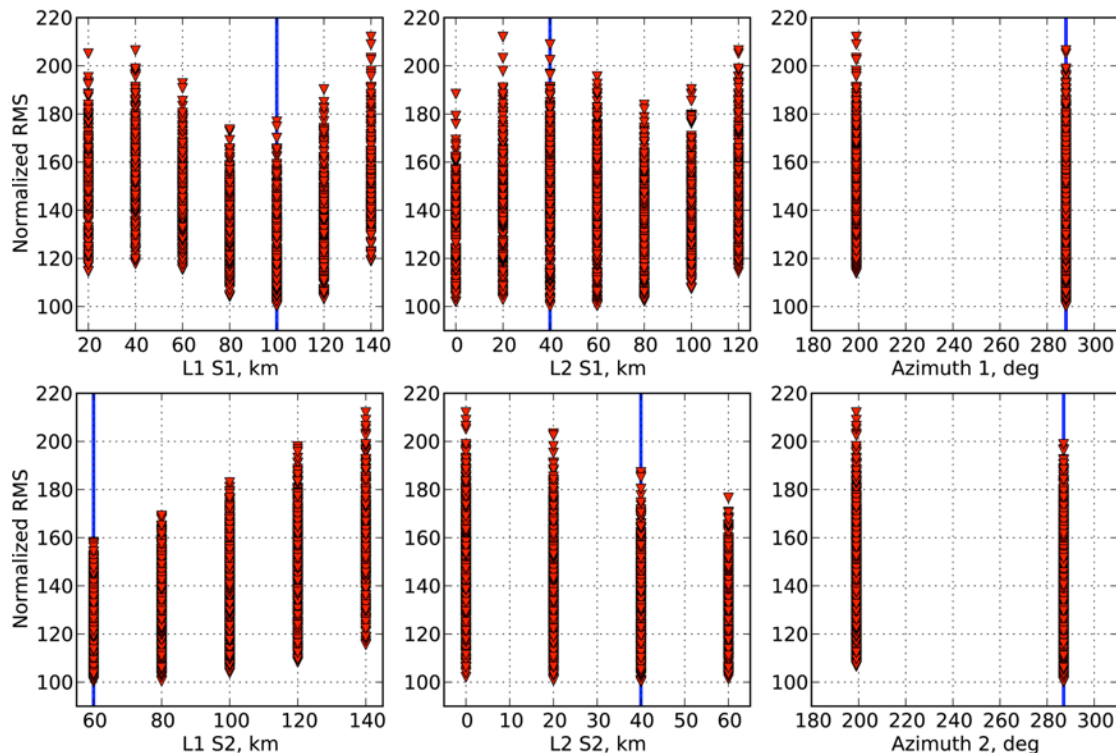
259 **Figure S17: Examples of observed and predicted surface-waves radiation**
 260 **patterns for simple rupture models (uniform slip, horizontal rupture**
 261 **propagation).** Comparison of observed (red circles) and predicted (blue
 262 triangles) equalized amplitudes for R1, R2 (middle) and G1, G2 (right). **a.** Single-
 263 point-source model. **b.** Two-point-source model. **c.** Optimum model with two
 264 parallel WNW-ESE bilateral ruptures. **d.** Example of two orthogonal NNE-SSW
 265 and WNW-ESE bilateral ruptures. **e.** Example of two parallel NNE-SSW bilateral
 266 ruptures.

267

268

269

270



271

272 **Figure S18: Summary of explored finiteness parameters for the Mw=8.6**

273 **2012 Sumatra earthquake.** Rupture lengths (L1 and L2) and azimuths are
274 regularly sampled for source I (first subevent, top 3 panels) and for source II
275 (second subevent, lower 3 panels). Blue lines indicate the optimum set of
276 parameters.

277

278

279